Wright State University
CORE Scholar

Browse all Theses and Dissertations | Theses and Dissertations

2012

Evaluation of Interpolation and Registration Techniques in Magnetic Resonance Image for Orthogonal Plane Super Resolution Reconstruction

Amir Pasha Mahmoudzadeh
Wright State University

Follow this and additional works at: https://corescholar.libraries.wright.edu/etd_all

 Part of the Biomedical Engineering and Bioengineering Commons

Repository Citation

Mahmoudzadeh, Amir Pasha, "Evaluation of Interpolation and Registration Techniques in Magnetic Resonance Image for Orthogonal Plane Super Resolution Reconstruction" (2012). *Browse all Theses and Dissertations*. 810.
https://corescholar.libraries.wright.edu/etd_all/810

This Thesis is brought to you for free and open access by the Theses and Dissertations at CORE Scholar. It has been accepted for inclusion in Browse all Theses and Dissertations by an authorized administrator of CORE Scholar. For more information, please contact library-corescholar@wright.edu.

EVALUATION OF INTERPOLATION AND REGISTRATION TECHNIQUES IN MAGNETIC RESONANCE IMAGE FOR ORTHOGONAL PLANE SUPER RESOLUTION RECONSTRUCTION

A thesis submitted in partial fulfillment of the
requirements for the degree of
Master of Science in Engineering

By

Amir Pasha Mahmoudzadeh

2012
Wright State University

Copyright by Mahmoudzadeh, A.P.

December 2012

WRIGHT STATE UNIVERSITY

GRADUATE SCHOOL

December 12, 2012

I HEREBY RECOMMEND THAT THE THESIS PREPARED UNDER MY SUPERVISION BY Amir Pasha Mahmoudzadeh ENTITLED Evaluation of Interpolation and Registration Techniques in MR Images for Orthogonal Plane Super Resolution Reconstruction BE ACCEPTED IN PARTIAL FULFILLMENT OF THE REQUIREMENTS FOR THE DEGREE OF Master of Science in Engineering.

_____

Nasser H. Kashou, Ph.D.
Thesis Director

_____

Thomas N. Hangartner, Ph.D.
Chair, Department of Biomedical, Industrial and Human Factors Engineering

Committee on
Final Examination

_____

Nasser H. Kashou, Ph.D.

_____

Ping He, Ph.D.

_____

Julie A. Skipper, Ph.D.

_____

Andrew Hsu, Ph.D.
Dean, Graduate School

ABSTRACT

Mahmoudzadeh, Amir Pasha, M.S.Egr, Department of Biomedical, Industrial, and Human Factors Engineering, Wright State University, 2012. Evaluation of Interpolation and Registration Techniques in Magnetic Resonance Image for Orthogonal Plane Super Resolution Reconstruction.

Super resolution reconstruction (SRR) combines several perspectives of an image (typically low resolution) in order to reconstruct a more complete and comprehensive (higher resolution) image. The aim is to use this concept on magnetic resonance imaging (MRI) data, for which the standard is to scan in several-plane orientation in a 2D fashion. As a result, clinical MRI, functional MRI (FMRI), diffusion weighted imaging (DWI)/diffusion tensor imaging (DTI), and MR angiography (MRA) tend to have high in-plane resolution but low resolution in the slice-select direction. By combining the 2 scans of the orthogonal plane, new 3D images can be reconstructed. This thesis addresses the principal problem of image quality and considers a novel SRR technique that uses the original information from 3 MRI plane orientations in order to enhance the resolution based on prior knowledge of scanning protocol as it relates to *voxel* resolution. The procedure for validating the MRI data algorithm is executed using MRI dataset of a human brain. The mean squared error (MSE) and peak signal-to-noise ratio (PSNR) were computed for quantitative assessment, whereas the qualitative assessment was performed by visually comparing the SR images to the original HR.

Keywords: Super resolution reconstruction, Image enhancement, MR Image

Tables of Contents

List of Figures

List of Tables

ACKNOWLEDGMENT

I would like to take this opportunity to extend my thanks to Almighty God who gave me health and strength and enabled me to accomplish this task successfully, and I would like to thank to my mother (Shokufeh Maabi) and father (Dr. Mohammad Reza Mahmudzadeh MD, MS) for their unconditional love and support, motivation, and guidance. Without them, I would not be where I am today. I love you mum and dad. My sincere thanks and gratitude go to my supervisor, Dr. Nasser H. Kashou (Ph.D.), for his constant support, understanding, and guidance throughout the year. It has been an absolute pleasure being one of your students. Thanks NK. I would like to thank Dr. Mohammad Ali Saghiri (Ph.D.) for his advice and encouragement during my Bachelor and Master degrees.

DEDICATION

I dedicate this dissertation:

To Forouzandeh ghazi: Your heart is bound together with mine for eternity. I feel it even when I'm a world away. Thanks for being my words when I had lost mine.

1 Introduction

1.1 Super Resolution Reconstruction (SRR)

Super Resolution Reconstruction (SRR) is the process of attaining several low-resolution (LR) images and combining them to achieve a high-resolution (HR) image [1], Figure 1. SRR plays a critical role in various applications such as electronic imaging, satellite mapping, military applications (e.g., target recognition), in waddition to medical imaging. In medical imaging the ability to reconstruct HR images is useful to a physician for making a correct diagnosis by better detecting brain tumors or pathological changes. In satellite images, an object can be discriminated more easily from similar objects utilizing HR images reconstructed from LR images of different scenes.

Figure 1: Combining low-resolution (LR) images to achieve a high-resolution (HR) image to achieve super resolution (SR) image construction.

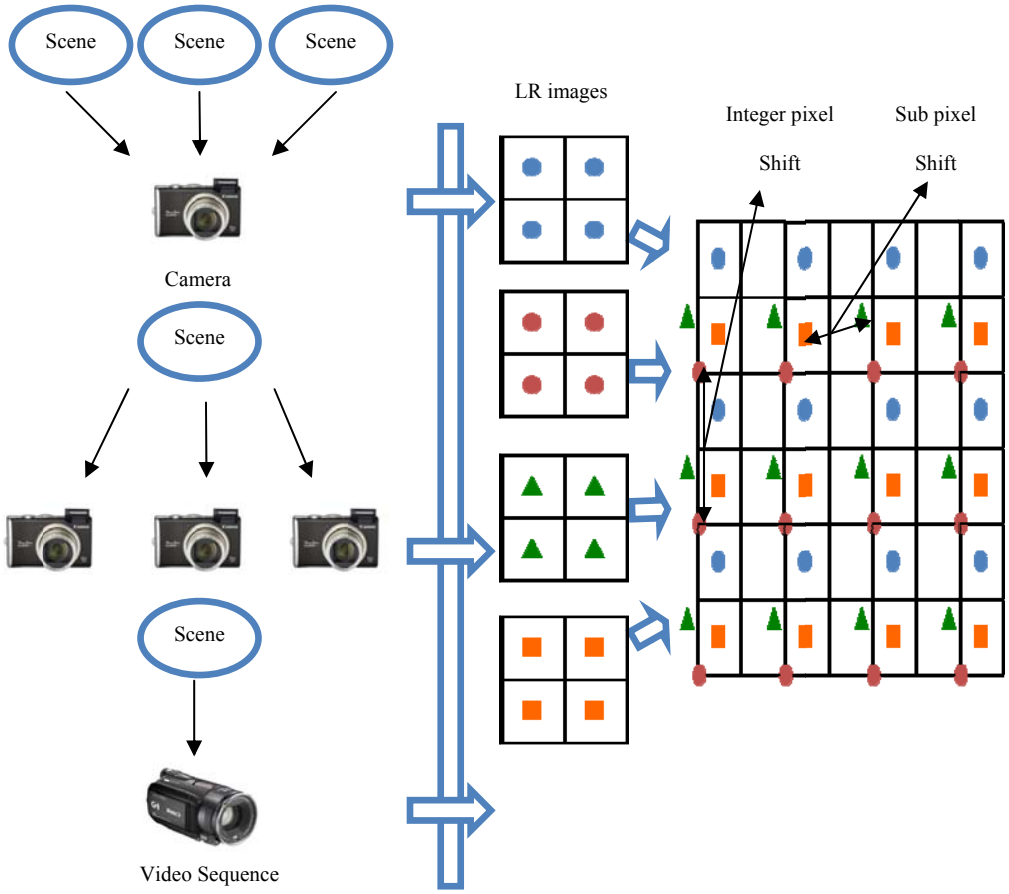

Figure 2: Basic conditions for super resolution. Multiple scenes can be acquired from one camera with several captures or from multiple cameras located in different positions. The red and blue circles, green triangle, and orange square represent the LR image (adapted from Park, Kang, Signal Processing Magazine, IEEE , vol.20, no.3, pp. 21- 36, May 2003 [1]).

These LR images are usually shifted in space such that one image contains data that the other does not. Acquiring multiple scenes can be through the use of one camera source with several captures or from several camera sources placed in different positions. The basic conditions for super resolution are shown in Figure 2. Another approach more applicable in magnetic resonance imaging (MRI) is to utilize the concept of acquiring LR

images from different scanning planes/perspectives (axial, sagittal, coronal) [2-3]. The major advantage of the combination of MRI data from three planes is that it will allow both visualization and data analysis of smaller areas than by using only one plane of orientation.

1.2 Observation Model

In the absence of gold standards, simulations are sometimes used to assess SRR accuracy. A common tactic is to take real data and deform it using an appropriate spatial transformation model (Affine, Rigid, Projective) and other factors thought to be relevant in limiting SRR accuracy, such as simulating the addition of noise and blurring. An observation model describes the process of obtaining a LR image from a HR image. The LR image can be obtained from warping, subsampling, blurring, and noise operators executed on the HR image. The observation model can be defined as [4-5]:

$$Y_k = D_k B_k G_k X + E_k \qquad k = \{1 \dots N\}, \tag{1.1}$$

where X is the ideal undegraded HR image, D_k represents a decimation operator for the k_{th} image (sub-sampling), G_k is the geometric transformation operator for the k_{th} image, B_k represents the blur operator of the k_{th} image, and E_k is the random sensor noise. A block diagram for this observation model is shown in Figure 3.

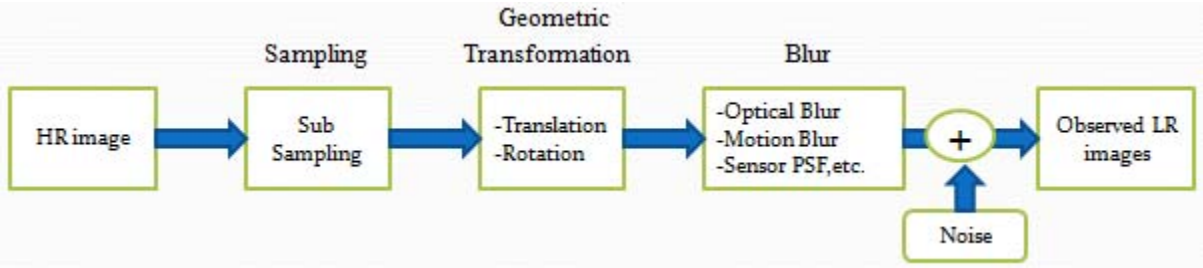

Figure 3: Observation model relating LR images to HR images. The LR image can be obtained from subsampling, warping, blurring, and noise operators executed on the HR image (adapted from Park, Kang, Signal Processing Magazine, IEEE , vol.20, no.3, pp. 21- 36, May 2003 [1]).

1.3 Super Resolution Algorithms

I will review a variety of super-resolution methods on previous and current work. First, I will discuss the maximum a-posteriori (MAP) super-resolution method, which has been used for SRR of MRI images. Then, I will discuss Irani and Peleg's approach. It should be noted that many current super-resolution algorithms are based on the work by Irani and Peleg [4-5]. There are many great sources for in-depth discussions of reconstruction of high resolution image from several LR MR scans [6-10].

1.3.1 MAP Super-resolution Image Reconstruction

The MAP super-resolution image reconstruction of two orthogonal planes was investigated by Bai, Han, and Prince [11]. They investigated the combination of two orthogonal planes (axial and coronal) in order to create a HR image based on a MAP super-resolution method with improved resolution of in-plane resolution in all directions

as well as improved SNR. In this section, I briefly summarize the MAP super-resolution reconstruction method [8-10].

SRR techniques typically start with an observation model (see Equation 1.1). A MAP method to find the best fit of X, denoted by X_{MAP}, which intends to maximize the a-posteriori probability, P, where K represents of the total number of LR observations and it is assumed that the K observations are independent of each other [11]:

$$X_{MAP} = \arg max_x \left[\mathrm{P}\{\mathrm{X}|\mathrm{Y}_1, \ldots, \mathrm{Y}_\mathrm{k}\}\right] \tag{1.2}$$

We can obtain the following equation by applying Bayes rule, and through some standard derivations [11]:

$$X_{MAP} = \arg max_x \left[\sum_{K=1}^{K} logP\{Y_k|X\} + logP\{X\}\right], \tag{1.3}$$

where $logP\{Y_k|X\}$ is the *log-likelihood* function for the k_{th} observation. $logP\{X\}$ is the logarithm of the *a-priori* probability distribution of X.

If it is assumed that typical noise in MR images is Gaussian, and the Markov random field (MRF) model as the prior distribution for $P\{X\}$can be modeled by the following equation [11-12]:

$$X_{MAP} = \arg min_x J(X), \tag{1.4}$$

where

$$J(X) = \frac{1}{\lambda}\int v_X(s)ds + \sum_{K=1}^{K}\frac{1}{\sigma_k^2}\int Y_K(s) - X(\,G_k(s)) \times B_k(s) \times D_k(s)ds, \tag{1.5}$$

where λ is the temperature parameter for MRF model and $v_X(s)$ is its local potential function. σ_k^2 is the standard deviation of Gaussian noise for k_{th} observation.

1.3.2 Irani and Peleg's Approach.

The approach by Irani and Peleg in reconstructing a HR image treats dynamic scenes and more complex motions than static scenes and pure translational motion in the image plane [5]. Their algorithm can create a set of simulated LR images. The image differences between the observed LR actual images and simulated LR images are back-projected. The back-projecting kernel can be used as an initial estimate of the HR image. The schematic diagram of the super-resolution algorithm is illustrated in Figure 4 [5].

The observed LR images sequences $\{g_k\}$ are obtained from the HR image. The imaging model can be expressed by the following equation:

$$g_k(m,n) = \alpha_k\left(h\left(T_k\big(f(x,y)\big)\right) + \eta_k(x,y)\right), \tag{1.6}$$

where g_k is the k_{th} observed image, f is the HR image that super-resolution algorithm is trying to find, T_k is the 2D geometric transformation that transform f to g_k. h is a blurring operator, which is specified by the Point Spread Function (PSF) of the sensor. η_k is an additive noise term, and α_k is a downsampling operator [5].

The super-resolution algorithm starts creating a higher resolution image with an initial guess f^0 for the HR image, and then imaging process is simulated to acquire a set of LR images. This simulated set of LR images $\{g_k^0\}_{k=1}^K$ corresponds to the set of observed images $\{g_k\}_{k=1}^K$ [5]. The imaging process of g_k at the n_{th} iteration can be expresses by the following equation:

$$g_k^{(n)} = (T_k(f^{(n)})*\mathrm{h}) \downarrow s, \tag{1.7}$$

where $\downarrow s$ is a down-sampling by a factor s, * is the convolution operator, and n is the n_{th} iteration.

If the initial estimate image f^0 is the correct HR image, then the simulated LR images $\{g_k^0\}_{k=1}^K$ must be equivalent to the observed LR images $\{g_k\}_{k=1}^K$. The difference between the images $\{g_k - g_k^{(0)}\}_{k=1}^K$ are computed and used to improve the initial guess image f^0 by back-projecting in order to acquire a HR image $f^{(1)}$. Each value in the difference image is back-projected onto its receptive field in the initial guess image. The following equation is repeated iteratively to minimize the error function [5].

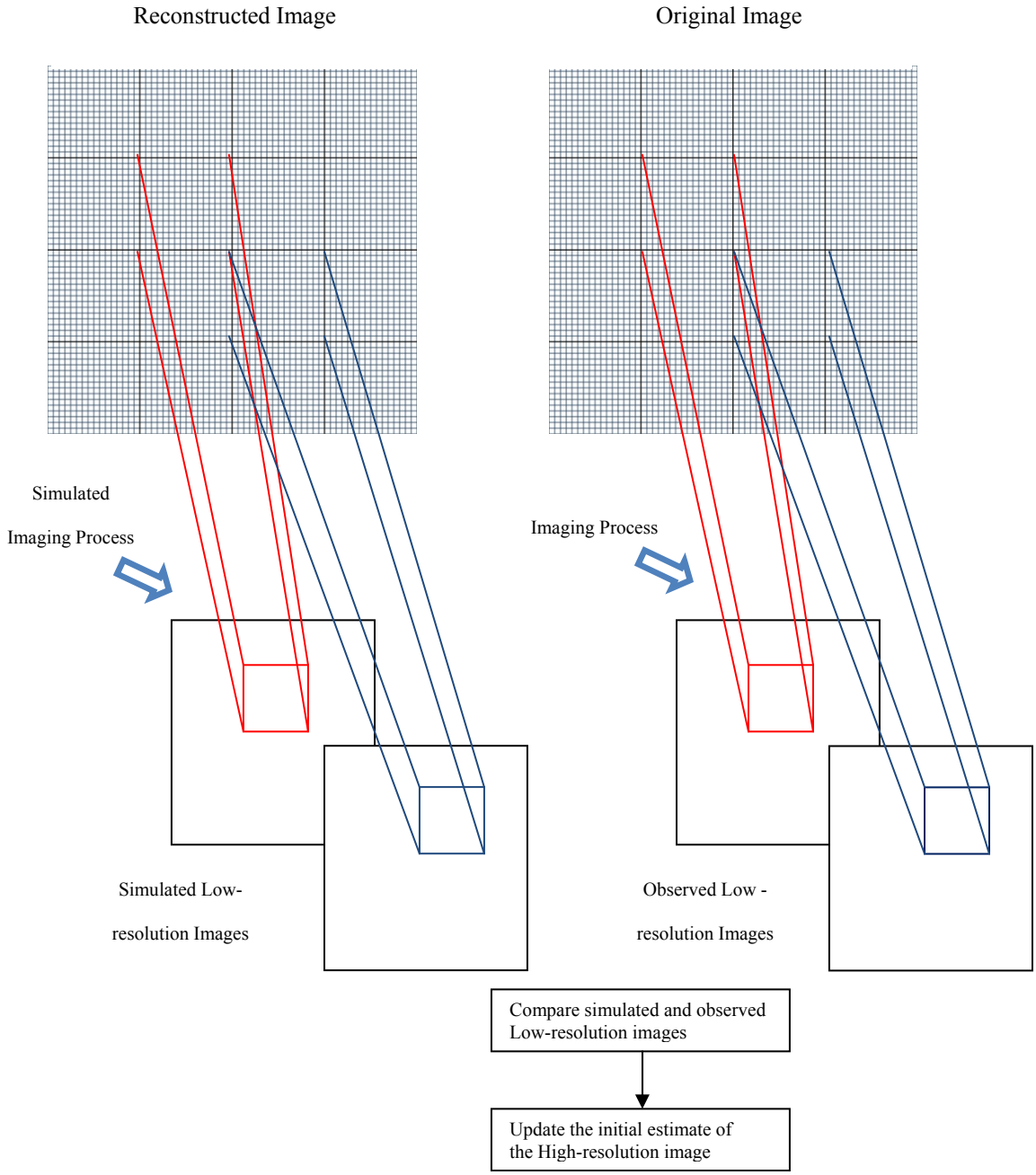

Figure 4: Schematic diagram of the super resolution algorithm proposed by Irani and Peleg. The initial estimate of the HR image is sought so that the simulated LR images are as close as possible to the observed LR images (adapted from Irani and Peleg, Journal of Visual Communication and Image Representation , vol.4, no.4, pp.324-335, 1993 [5]).

$$e^{(n)} = \sqrt{\frac{1}{K}\sum_{k=1}^{k} ||g_k - g_k^{(n)}||_2^2} \tag{1.8}$$

The iterative update scheme for the super-resolution process is defined by:

$$f^{(n+1)} = f^{(n)} + \frac{1}{k}\sum_{k=1}^{k} T_k^{-1}(\left(\left(g_k - g_k^{(n)}\right) \uparrow s\right) * p), \tag{1.9}$$

where k is the number of LR images, p is the back-projection kernel utilized to deblur the image, $\uparrow s$ is an up-sampling operator by a factor s, and * is the convolution operator [5].

1.4 Significance and hypothesis of Research

Standard clinical MRI images are acquired in 2D and in different orthogonal planes. Three orthogonal planes are revealed by the illustrations in Figure 5. The 2D multi-slice MR scans have high in-plane resolution, but the larger slice thickness and the use of slice gaps diminish the details that can be seen in the slice-select direction.

The main goal of this study was to use SRR on an orthogonal-plane clinical MRI to enhance image quality and recover data, and I hypothesized that combining the images

from the different planes would increase the quality of the dataset in comparison to only one-plane data.

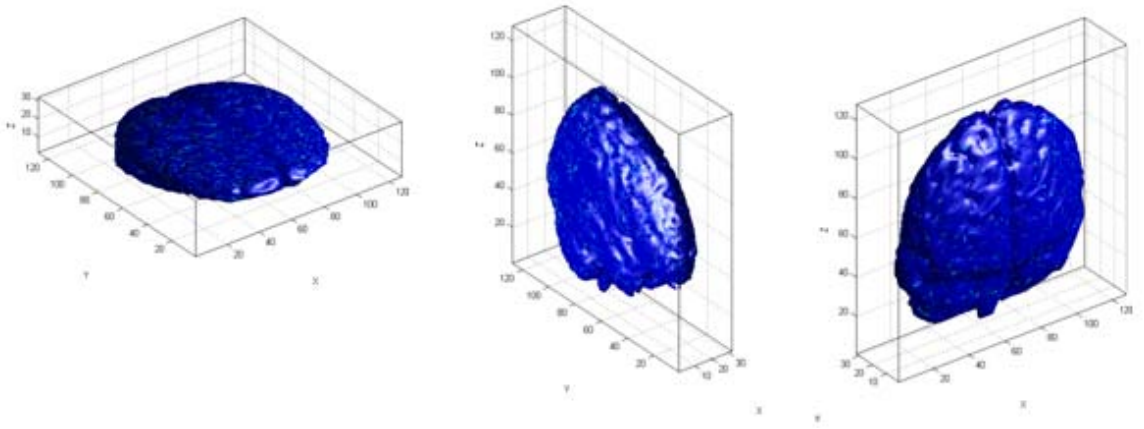

Figure 5: Three orthogonal planes are illustrated in the axial (left column), sagittal (middle column), and coronal (right column) views.

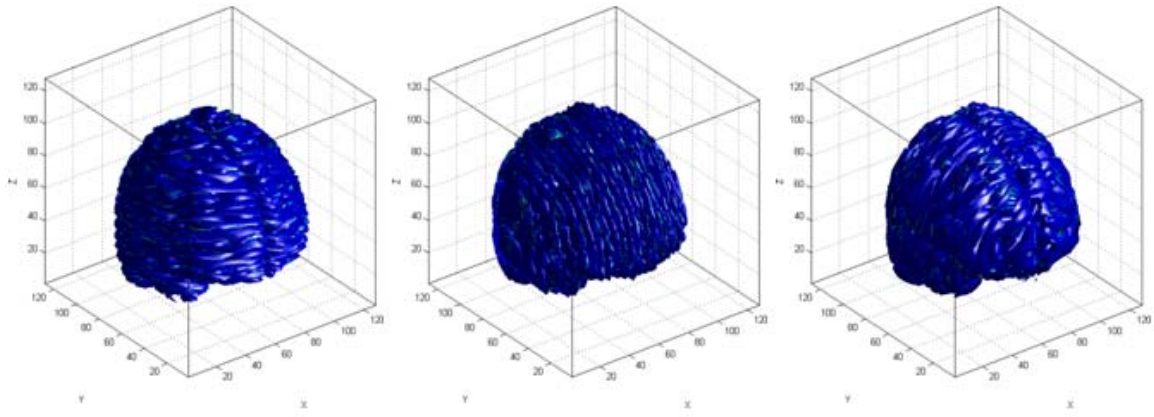

Figure 6: Each plane is mapped to common grid.

The combination of MRI data from three plane orientations will allow both visualization and data analysis of smaller areas than by using only one plane of orientation. It will also allow for an increase in signal-to-noise ratio (SNR) as a result of combining thicker *voxel*s. This is achieved by the fact that the in-plane resolution is commonly higher than the slice-select direction.

1.5 Organization of Thesis

The rest of the thesis is organized as follows: Chapter 2 shows an overview of MRI, interpolation, and registration in SRR. The third chapter of this thesis explains the methods and measurements. Chapter 4 presents a systematic evaluation of interpolation techniques, considering speed, accuracy, and robustness, and determines the best overall interpolation method. The study then focuses on interpolation effects on the accuracy of cost-function-based optimized automatic image registration. Chapter 4 concludes with the SRR results and with a discussion of the SRR technique. Finally, Chapter 5 concludes with a summary and a discussion of possible directions for future research.

2 Interdependence of MRI, Interpolation, and Registration in SRR

In this chapter, I lay the foundations for this study by discussing the structure of the brain and MRI basics, and then I discuss interpolation techniques and image registration processes, and their relation to the SRR. The aim is to expand understanding of interpolation and registration and to discover how they are involved with SRR.

2.1 Brain Structure

The human brain is one of the largest and most complex organs in the human body and is composed of three main parts: brain stem, cerebellum, and cerebrum (Figure 7). The brain stem is responsible for automatic survival functions, such as breathing, digestion, blood pressure, rate regulation, sweating, and the ability to sleep. All areas of the nervous system connect with the brain stem. The cerebellum is well known as the "little brain" and is responsible for muscle tone and balance, as well as nonverbal learning and memory. The cerebrum is the largest region of the brain and is responsible for memory, consciousness, movement control, vision, emotional response, and language [13].

Brain imaging allows visualization of brain structures, which is useful in diagnosis and surgery. For instance, information about bleeding, infection, defects, and tumors are gathered through brain imaging, and then surgery can be planned accordingly.

furthermore, researchers utilize brain imaging to study brain development in both healthy and ill people.

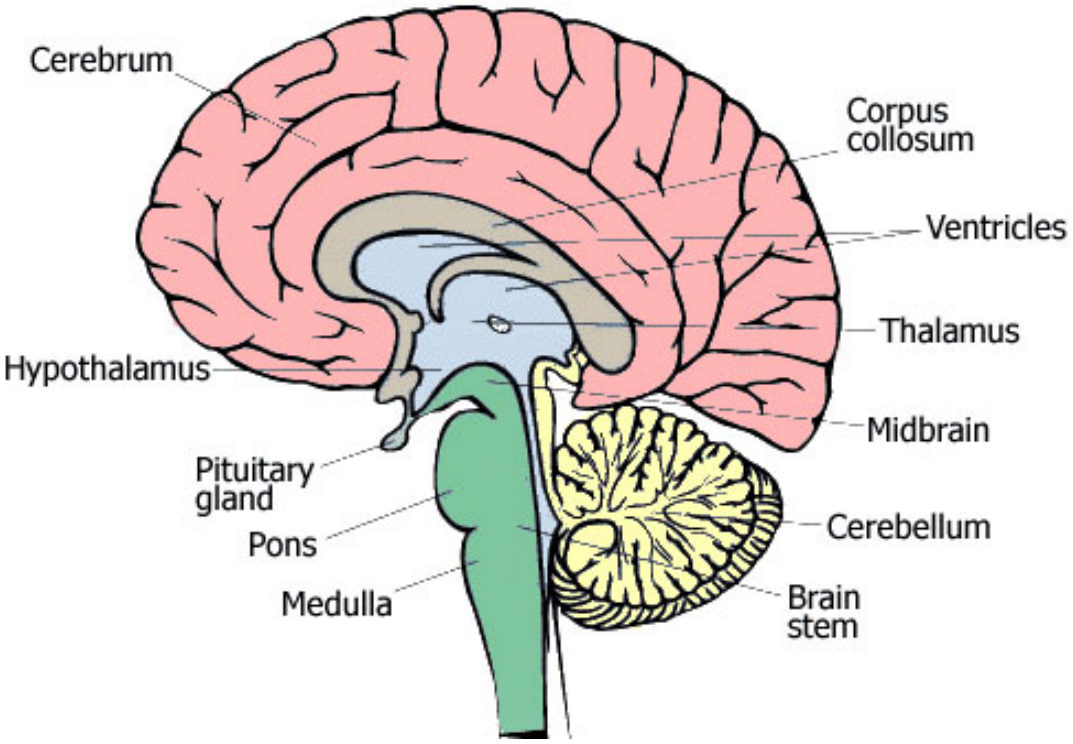

Figure 7: Basic human brain structure (obtained from web brain, Epliepsy Action Australia [13]).

2.2 MRI Basics

An MRI of the brain is a painless procedure that utilizes a magnetic field and radio waves to generate detailed images of the brain, and is useful as a tomographic imaging modality for generating images of a slice through the human body (see Figure 8). Before going into the scanning the brain, it is important to explain some basic

knowledge of MRI. The simple design of an MRI machine resembles a long horizontal tube. The metal tube contains a radio frequency (RF) coil, which sends and receives radio signals, and a series of magnetic coils (main magnetic coil, X magnetic coils, Y magnetic coils, and Z magnetic coils), which are each oriented along a different plane of the patient's body. The main magnetic coil is the most important component in an MRI system because it creates a uniform magnetic field, the X magnetic coils create a varying magnetic field from left to right, the Y magnetic coils create a varying magnetic field from top to bottom, and the Z magnetic coils create a varying magnetic field from head to toe (Figure 9). These magnets (X, Y, and Z coils) are far less powerful (18 to 27 millitesla) than the main magnet (0.5 to 3 tesla) [15-16]. The rest of an MRI system cons-

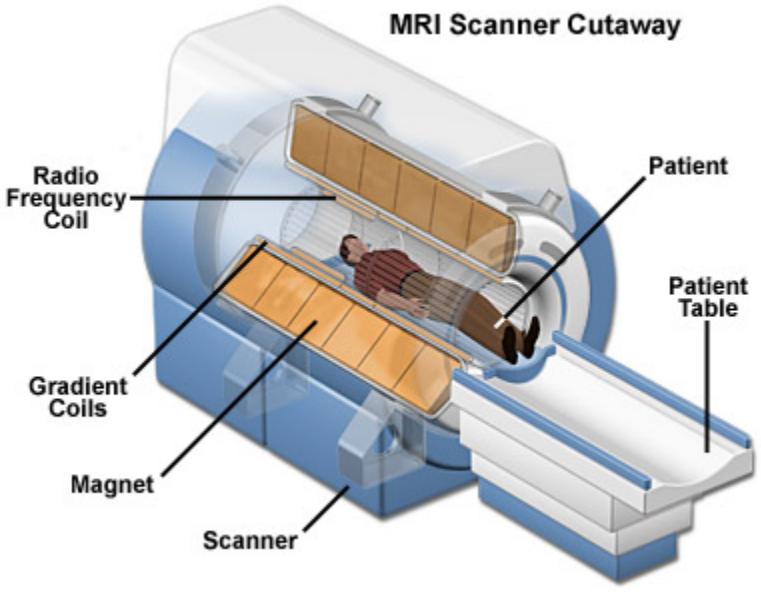

Figure 8: MRI Machine (obtained from Kristen Coyne, National High Magnetic Field Laboratory [14]).

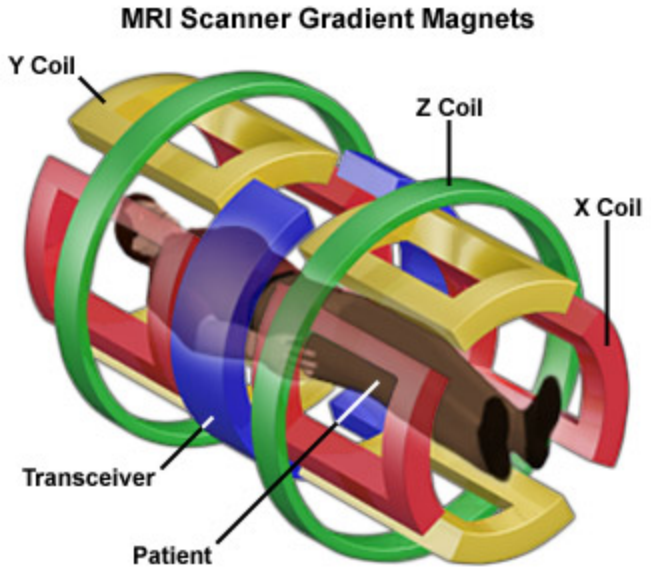

Figure 9: An MRI system contains a radio frequency (RF) coil, which sends and receives radio signals, X magnetic coils that create a varying magnetic field from left to right, Y magnetic coils that create a varying magnetic field from top to bottom, and Z magnet is coils that create a varying magnetic field from head to toe (obtained from Kristen Coyne, National High Magnetic Field Laboratory [14]).

-ists of a computer system the interprets the data received during the scan to create 2D and 3D images of the body, and some equipment that sends RF pulses into the patient's body. In order to understand how MRI machine works, I will explain a bit more about the human body. Our bodies are mainly made up of water. Water consists of 2 Hydrogen and 1 Oxygen atom. Hydrogen atoms are very sensitive to magnetic fields and, in understanding how the scanner affects them, you will understand how the machine works. Imagine a patient lying on the table inside the bore of the scanner. Before the main magnet is switched on, the millions of hydrogen atoms within our patient's body are spinning randomly or precessing in every direction. Once the MRI scanner is turned on,

the magnetic field runs straight down the center of the tube where the patient is laid and makes all the hydrogen protons line up in the direction of either the patients' head or the patients' feet [15]. The vast majority of these atoms (toward the feet and toward the head) will cancel each other out, but a few every million in the body are not canceled out (see figure10). Those unmatched (not canceled out) atoms in the body are what the MRI scanner uses to create its images.

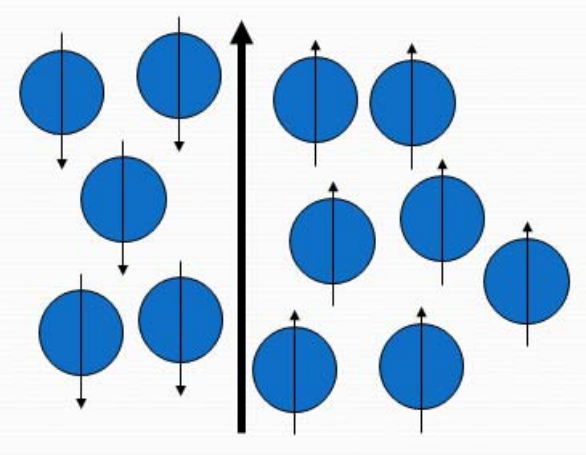

Figure 10: Some of the protons align with the field and some actually align against the field cancelling each other out, but, as illustrated here, there is one or two additional protons.

The secondary magnetic coils (X, Y, and Z) within MRI send out RF pulse. The pulse causes the protons in that area to absorb the energy required to make them spin in the opposite direction. Once the RF is turned off, the hydrogen protons spin back to their natural alignment within the magnetic field and release the energy just absorbed. This is the *resonance* part of MRI. When they do this, they transmit a signal that the coil now

picks up and sends to the computer system. What the system receives is signal that is changed into a picture. That is the imaging part of MRI [16].

MRI image quality is dependent on several factors such as repetition time (TR), echo time (TE), the number of signal averages (NA), and resolution. So how do these factors affect the images? How should we adjust these factors to get high contrast brain images? To find out answer of these questions, I need to explain some critical terms in MRI: T1 and T2. T1 is spin-lattice relaxation time which relates to the recovery of the magnetization along z direction after RF pulse. There is no magnetization along x and y directions here. T2 is spin-spin relaxation time which related to decay of magnetization in transverse plane after RF pulse [16]. A long TR allows for more slices to be obtained while decreasing T1 contrast and increasing scanning time. Therefore, to decrease the scanning time, TR can be decreased, which allows for more T1 contrast, but fewer slices and lower the SNR can be acquired. Increasing TE leads to more T2 weighting, but decreases in SNR. Scan time is directly to NA. SNR increases as NA is increased. Each slice has a thickness (ST) that can affect the resolution of the image, the received signal, and partial volume effects (PVE). For instance, changing the ST from 20 mm to 10 mm, results in a 50% loss of SNR. Thinner slices reduce PVE and increase resolution. Resolution is a function of the number of frequency encode (FE) steps, the number of phase encode (PE) steps, slice thickness, and field of view (FOV). In-plane resolution is improved as FE and PE steps are increased. The smaller the FOV is, then the higher the resolution, and the smaller the *voxel* size [17]. The slice is composed of several volume

or element *voxels*. The MRI image is composed of several picture elements called pixels. The intensity of a pixel represents the MRI signal intensity of the corresponding object *voxel* being imaged. In this research, I am mostly concerned with the resolution and SNR components.

Commonly, brain views are shown in one of three perspectives. The transverse (axial or x-y) planes slice the patient from top to bottom, the sagittal (y-z) planes slice the patient laterally, and the coronal (x-z) planes slice the patient lengthwise from front to back (Figure 11). Different slice selection directions are utilized to obtain an image volume. Axial, sagittal, and coronal planes in the brain MRI volume consist of 2D slices. Each 2D image is considered a slice plane, whereas the slice selection direction is oriented along the Z-axis. As illustrated in Figure 12, the resolution in the slice selection direction is lower than that of the in-plane direction [18].

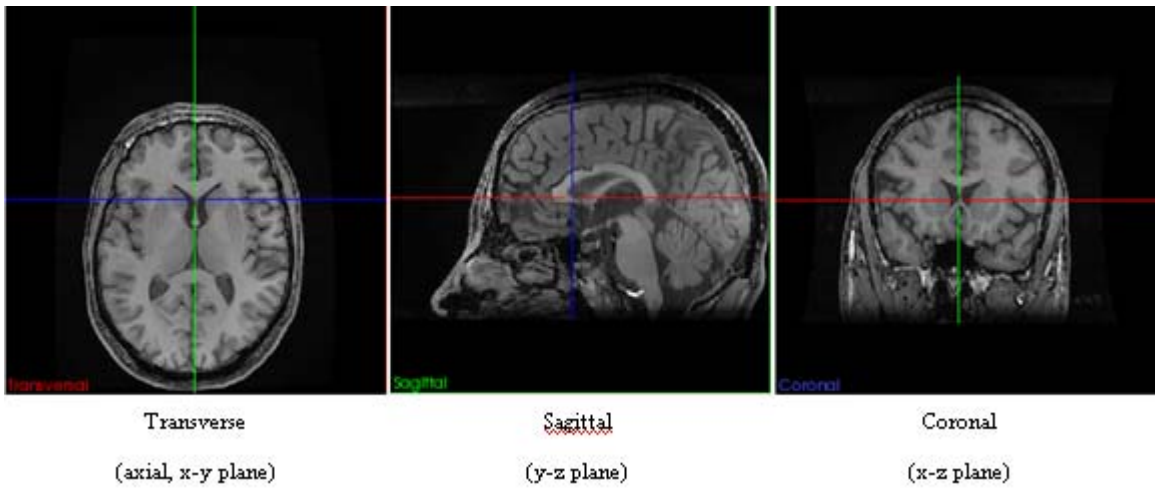

Figure 11: Three perspectives of the brain.

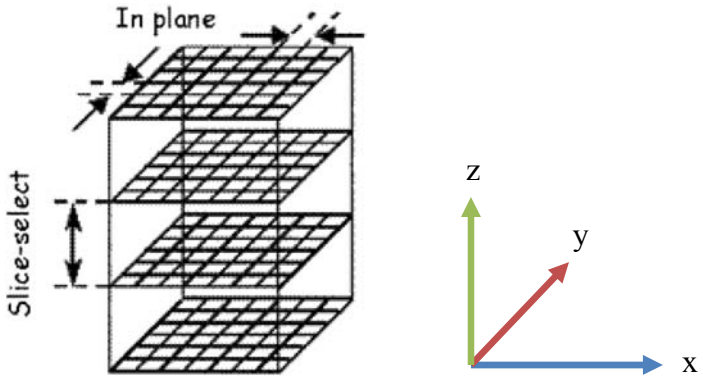

Figure 12: MRI slice acquisition. The z-axis is selected along the slice-selection direction, and the y- and x- axes coincide with the phase- and frequency-encoding directions, respectively (obtained from Greenspan , Oz , Kiryati , Peled, Magnetic Resonance Imaging, vol.20, pp. 437-446, 2002 [18]).

2.3 Interpolation

Interpolation has become a default operation in image processing and medical imaging and is one of the important factors in the success of SRR. Interpolation is needed if the fractional unit of motion is not matched and located on the HR grid. One scheme for the interpolation step is shown in Figure 13. Here, a circle shows the reference HR image, and a diamond and a triangle represent a shifted HR pixel. For instance, if the image is down-sampled by a factor of 4, a diamond has (0.25, 0.25) sub-pixel shift for the vertical and horizontal directions and a triangle has a shift that is less than (0.25, 0.25). In Figure 13, a triangle is not placed on the HR grid and it needs interpolation, but a diamond does not need interpolation. Some interpolation approaches are proposed to overcome the problem of low resolution in medical imaging. MRI is an invaluable

modality in the medical field. Particularly, neuroimaging with MRI helps physicians to study the internal structure and functionality of the human brain. In these cases, high resolution and isotropic images are important because higher isotropic resolution could theoretically reduce partial volume artifacts, leading to better accuracy/precision in deriving volumetric measurement and decreasing considerable errors in registration [19]. Clinically, acquiring a fully isotropic 3D image set is not feasible because of time, motion artifacts, and SNR factors. Thus typically, in 3D MR data, the in-plane direction has higher resolution than the slice direction (z-axis). In this case, invaluable information will be lost in the latter direction. The objective is to recover and fill in this missing information in order to enable the physicians to obtain a more accurate perspective of the

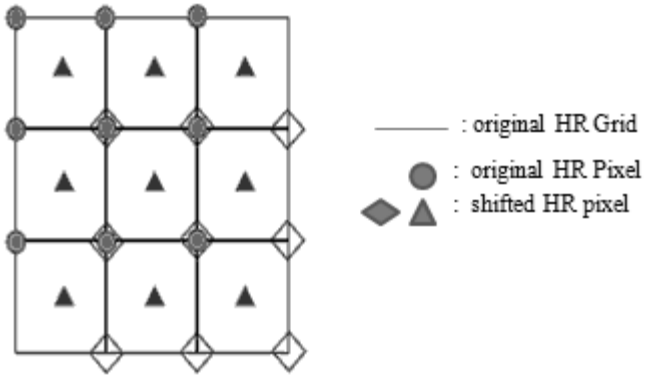

Figure 13: Scheme for interpolation. Straight line shows the original HR grid, circle shows the reference HR image, and a diamond and a triangle represent a shifted HR pixel (obtained from Park, Kang, Signal Processing Magazine, IEEE, vol.20, no.3, pp. 21- 36, May 2003 [1]).

underlying structure available in the data by optimizing the choice of interpolation techniques. The study of interpolation approaches date back to the 1980s [20]. A great diversity of techniques can be found in the literature of the 1980s: For example, B-splines

were sometimes referred to as *cubic splines* [21], whereas cubic interpolation was also known as *cubic convolution* [22-24], and as *high resolution spline interpolation* [25]. In this section, eight interpolation algorithms are reviewed, including cubic Lagrangian, quintic Lagrangian, and heptic Lagrangian. Furthermore, I explain the nearest neighbor interpolation approach, which is associated with strong aliasing and blurring effects. Furthermore, discussions of the trilinear interpolation approach as well as B-spline 3rd order, B-spline 4th order, and windowed Sinc are included. Different 2D interpolation approaches exist in medical imaging [22], [26]. In chapter 4, I discuss and evaluate the performance of these interpolation algorithms in order to find the best interpolation method for high accuracy of super resolution image reconstruction.

2.3.1 Lagrange Interpolation

Lagrange interpolation is a famous, classical technique for interpolation. The Lagrange interpolation is way to pass a kernel of degree N-1 through N x N points and is defined in X direction (for 2D image, adds Y direction, and for 3D image, adds Y and Z directions) [23-31],

$$Lagra_{hn(x)} = \begin{Bmatrix} \prod_{j=0, j-\frac{N}{2}+1\neq n}^{N-1} & \frac{n-i-x}{n-i}, n-1 \leq x < n \\ 0, & elesewhere \end{Bmatrix}, \quad (2.1)$$

where $i=j-\frac{N}{2}+1$, and $n\in\left\{-\frac{N}{2}+1,-\frac{N}{2}+2,\ldots,\frac{N}{2}\right\}$ are the Lagrange kernels. The Lagrange kernel for N=1 equals the nearest neighbor interpolation. In this case, N=2 equals the linear interpolation. The Lagrange kernels for N=4 and N=5 supporting points result in cubic and quartic polynomials, respectively, and are shown in Equations 2.2 and 2.3:

$$Lagra_{h4(x)}=\begin{cases}\frac{1}{2}x^3-x^2-\frac{1}{2}x+1, & for\ 0\le x<1\\ \frac{-1}{6}x^3+x^2-\frac{11}{6}x+1, & for\ 1\le x<2\\ 0, & elsewhere\end{cases} \tag{2.2}$$

$$Lagra_{h5(x)}=\begin{cases}\frac{1}{4}x^4-54x^2+1, & for\ 0\le x<{}^1\!/_2\\ \frac{-1}{6}x^4+\frac{5}{6}x^3-\frac{5}{6}x^2-\frac{5}{6}x+1, & for\ {}^1\!/_2\le x<{}^3\!/_2\\ \frac{1}{24}x^4-\frac{5}{12}x^3+\frac{35}{24}x^2-\frac{25}{12}x+1, & for\ {}^3\!/_2\le x<{}^5\!/_2\\ 0, & eleswhere\end{cases} \tag{2.3}$$

2.3.2 Nearest Neighbor Interpolation

Nearest Neighbor interpolation (also known as Zero-order interpolation) is the simplest method, and strong aliasing and blurring effects are associated with this interpolation [32]. The local 1-point Lagrange interpolation is equivalent to the nearest-neighbor interpolation, defined by equation 2.4:

$$w(x,n) = \begin{cases} 1, & for \quad n - \frac{1}{2} \le x < n + \frac{1}{2} \\ 0, & otherwise \end{cases} \tag{2.4}$$

The images when scaled up in size may look very blocky. Likewise, the local 2-point Lagrange interpolation is equivalent to the linear interpolation, defined by equation 2.5:

$$w(x,n) = \begin{cases} 1 - |x - n|, for & n - 1 \le x < n + 1 \\ 0, & otherwise \end{cases} \tag{2.5}$$

2.3.3 Trilinear Interpolation

Trilinear interpolation calculates values placed between existing *voxel* values by linearly weighting the eight closest neighboring values. In other words, trilinear is the name given to the process of linearly interpolating points within a 3D box, given the values at the vertices of the box [33].

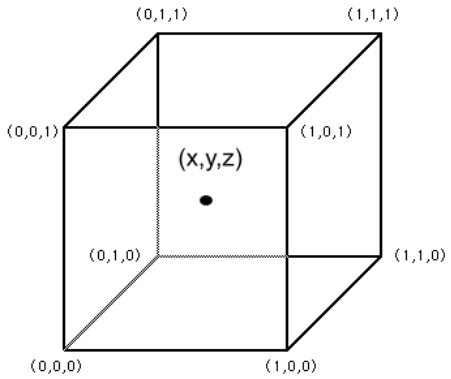

Figure 14: Trilinear interpolation computes values located between existing *voxel* values by linearly weighting the eight closest neighboring values (obtained from National Institutes of Health Center for Information Technology, Rockville, MD. [33]).

The known values at each vertex is indicated V000, V100, V010, ..., V111, and the unknown value is calculated by merging the known corner values weighted by their distance from the point (x, y, z) within the cube.

2.3.4 B-spline interpolation

B-spline interpolation uses weighted *voxel* values in a wider neighborhood compared to trilinear interpolation, but both the B-spline and Trilinear kernels are symmetrical and separable. The place of the neighboring points as control points relates to B-spline interpolation and combines the intensity values at these places using a set of polynomial basis according to equation 2.6 [34].

Equation 2.6 shows k-order B-spline with n control points (P1, P2, ... , Pn),

$$P(t)=\sum_{i=1}^{n+1} N_{i,k}P_i,\ t_{min} \leq t < t_{max} \tag{2.6}$$

In equation 2.6, $N_{i,k}$ are the polynomial functions of degree k-1, and n is the number of control points; k must be at least 2 (linear), and less than n+1. It is important to note that the degree of the weighting polynomial is separate from the number of control points, n [33].

The weighting polynomial can be recursively defined by the following equation [34],

$$N_{i,k}=\frac{t-t_i}{t_{i+k-1}-t_i}N_{i,k-1}(t)+\frac{t_{i+k}-t}{t_{i+k}-t_{i+1}}N_{i+1,k-1}(t) \tag{2.7}$$

In equation 2.7, t(i) represents an index that refer to the control points and t(i) are generally referred as knot points (see Figure 15).

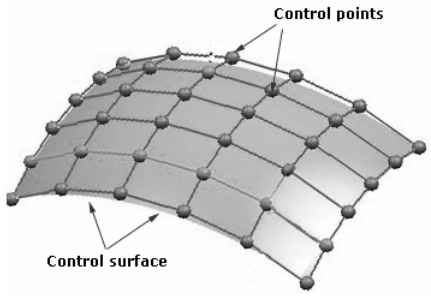

Figure 15: B-spline interpolation. There are n control point[s] (P1, P2, ... , Pn). The sequence of the control point is called a *control surface* (obtained from National Institutes of Health Center for Information Technology, Rockville, MD. [33]).

The series of control point is defined as a control surface. According to Spitzer, Nie, Du, Mei and McAullife, "This indexing scheme allows one to weight different control points more than other control points by using one more than once during the computation. Typically, the first and last control points are weighted more heavily than the internal points to give a smooth interpolating curve." [21], [23], [25-26], [33-35].

2.3.5 Windowed Sinc Interpolation

This interpolation function has minimum aliasing artifacts in contrast to linear interpolation. Sinc function can be windowed more generally to yield [23], [27]:

$$Sinc(x) = \begin{cases} \frac{sin\,(x)}{x}, & \forall x \neq 0 \\ 1, & x = 0 \end{cases} \quad (2.8)$$

Think of an image data set comprising a 3D matrix *voxel* with intensities I(X,Y,Z), specified by integer position coordinates (X,Y, Z). If one wants to calculate the intensity value at an interior point defined by non-integer coordinates (X,Y, z), this can be obtained by the following equation [23]:

$$I(x,y,z) = \sum_X \sum_Y \sum_Z I(X,Y,Z) Sinc\big(\pi(x-X)\big) Sinc\big(\pi\,(y-Y)\big) Sinc\big(\pi(z-Z)\big) \quad (2.9)$$

For satisfying equation 2.9, two limiting conditions are required:

- I(x,y,z) must be band limited.
- The sampling rate –fs, must be greater than twice the bandwidth, e.g.fs>2B.

The following section discusses the registration process and explains how registration is involved with SRR.

2.4 Image Registration Algorithms

Registration is a critical step to the success of SRR. Therefore, the minimum registration error is needed. Image registration methods in medical imaging seek to align two or more images and can be applied in the same modality on the same patient for the purpose of monitoring and quantifying disease progression over time. Registration can also be applied across different modalities, which is useful for correction of different patient positions across scans, for instance, aligning Positron Emission Tomography (PET) data to an MRI image. Also, image registration can be used on the different patients, which is useful for studies of variability between subjects. Image registration is classified into the following categories and depends on several factors: image modalities (MRI, PET, CT, etc), the subject of registration (a single person or different persons), the object of registration (head or heart), the image dimensionality (e.g., 2D, 3D, and 4D), and geometrical transformation (affine, rigid, projective, etc).

This study focuses on an intensity-based registration method. In this registration, interpolation, geometric transformation, and cost function assessment are essential steps, as they can affect the accuracy of registration. This section examines 3D affine registration of brain images using *voxel* intensities similarity measures such as Normalized Mutual Information (NMI), Normalized Cross Correlation (NCC), Least squares (LS), and Correlation Ratio (CR). More explicitly, if a target image is re-sampled to match a reference image, the image intensities at each *voxel* should be similar in the two images. In fact, when utilizing an intensity-based cost function, it is essential to

repeatedly re-sample one of the images to match the other at several various resolutions, while searching for the min cost function. This re-sampling process requires interpolation during the registration process [39]. In Optimized Automatic Registration Image (OAIR) method, interpolation involves re-sampling of anisotropic *voxel*s in the Z-direction into isotropic cubic *voxel*s. Also, it is important to note that in the OAIR method, the interpolation technique utilized for registration does not necessarily need to be the same interpolation technique used during registration to compute a final image using the optimal parameters.

2.4.1 Geometric Transformation

When registering images, one should specify a geometric transformation that specially aligns one image to another. The transformation can be classified as rigid, affine, and projective. Rigid transformation can be defined as a simple transformation that includes only translation and rotation. The projective transformation is the most general transformation and maps lines to lines (but does not necessarily preserve parallelism). An affine transformation includes scaling, rotation, translation, shearing, and reflection. There are several scanner-produced errors that can result in skewing or scaling terms, and affine transformations are applied to overcome these problems.

An affine transformation maps straight lines to straight lines and keeps the parallelism of lines, but not their lengths or their angles. Changing scaling and shearing factors for each image dimension will extend the degree of freedom (DOF; the number of

independent pieces of information that go into the estimate of a parameter) of the rigid transformation [40-47]. Figure 16 shows the five basic components of affine transformations.

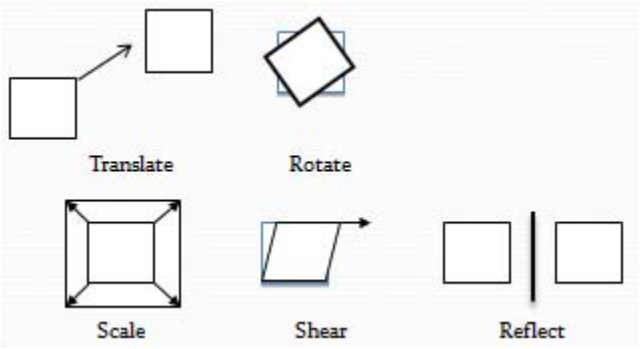

Figure 16: The five basic affine transformations are translate, rotate, scale, shear, and reflection. *Translate* moves a set of points a fixed distance in x- and y-directions, *Rotate* rotates a set of points about the origin, *Scale* scales a set of points up or down in x- and y-directions, and *Shear* offsets a set of points a distance proportional to their x- and y-coordinates. *Reflection* produces a mirror image of set of points in x- or y-directions.

The following matrices constitute the basic affine transforms in 3D, addressed in homogeneous form.

Translation:

Translate a point in the xy-plane to a new place by adding a vector (a, b). $\mathbf{x}'=x+a$ and $\mathbf{y}'=y+b$. $\mathbf{P}'$ represents of translated matrices.

$$\mathbf{T}(t_x, t_y, t_z): \quad \begin{bmatrix} 1 & 0 & 0 & t_x \\ 0 & 1 & 0 & t_y \\ 0 & 0 & 1 & t_z \\ 0 & 0 & 0 & 1 \end{bmatrix}, \tag{2.10}$$

$\mathbf{P}' = \mathbf{TP}$, where,

$$\mathbf{P}' = \begin{bmatrix} x' \\ y' \\ z' \\ 1 \end{bmatrix}, \quad \mathbf{P} = \begin{bmatrix} x \\ y \\ z \\ 1 \end{bmatrix} \tag{2.11}$$

Scaling:

Scaling is making the new scale of a coordinate direction p times larger. Scaling is applied to all axes, each with a different scaling factor (s_x, s_y, s_z). $\mathbf{P}'$ represents of scaled matrices.

$\mathbf{P}' = \mathbf{SP}$,

$$\mathbf{S}(s_x, s_y, s_z): \quad \begin{bmatrix} s_x & 0 & 0 & 0 \\ 0 & s_y & 0 & 0 \\ 0 & 0 & s_z & 0 \\ 0 & 0 & 0 & 1 \end{bmatrix} \tag{2.12}$$

Rotation:

If a point (x, y, z) is rotated an angle θ about the coordinate origin to became a new point ($\mathbf{x}'$, $\mathbf{y}'$, $\mathbf{z}'$), the three basic rotations in 3D can be defined as follows:

Rotation about the x-axis:

$$\begin{bmatrix} x' \\ y' \\ z' \end{bmatrix} = \begin{bmatrix} 1 & 0 & 0 \\ 0 & \cos\theta & -\sin\theta \\ 0 & \sin\theta & \cos\theta \end{bmatrix} \begin{bmatrix} x \\ y \\ z \end{bmatrix} \tag{2.13}$$

Rotation about the y-axis:

$$\begin{bmatrix} x' \\ y' \\ z' \end{bmatrix} = \begin{bmatrix} \cos\theta & -\sin\theta & 0 \\ \sin\theta & \cos\theta & 0 \\ 0 & 0 & 1 \end{bmatrix} \begin{bmatrix} x \\ y \\ z \end{bmatrix} \tag{2.14}$$

Rotation about the z-axis:

$$\begin{bmatrix} x' \\ y' \\ z' \end{bmatrix} = \begin{bmatrix} \cos\theta & 0 & \sin\theta \\ 0 & 1 & 0 \\ -\sin\theta & 0 & \cos\theta \end{bmatrix} \begin{bmatrix} x \\ y \\ z \end{bmatrix} \tag{2.15}$$

There are several reasons for using homogeneous coordinates, including the ability to apply all four transformations multiplicatively. Because transformation combinations (shearing, scaling, and rotation) are all multiplicative transforms, whereas only translation is an additive transform. Equation 2.16 shows changing translation from additive transform into multiplicative transform using homogeneous coordinate.

$$\begin{pmatrix} y_1 \\ y_2 \end{pmatrix} + \begin{pmatrix} e \\ f \end{pmatrix} = \begin{pmatrix} y_1+e \\ y_2+f \end{pmatrix} \rightarrow \begin{pmatrix} 1 & 0 & e \\ 0 & 1 & f \\ 0 & 0 & 1 \end{pmatrix} \begin{pmatrix} y_1 \\ y_2 \\ 1 \end{pmatrix} = \begin{pmatrix} y_1+e \\ y_2+f \\ 1 \end{pmatrix} \tag{2.16}$$

In many cases, several transformations may be used to bring an object to its desired position. The product of all involved matrices can be summarized into a single transformation. For instance, a transformation $m=A_n$ may be needed to bring n to m, followed by a second transformation $s=B_m$ bringing m to s, followed by yet another transformation $t=C_s$ bringing s to t. These transformations can be summarized in the following transformation (A, B, C, D are all transformation matrices):

$$t = C_s = C(B_m) = CB_m = CB(A_n) = CBA_n = D_n \quad (2.17)$$

In the following example, the following transformation is applied to the image:

1. Scaling in the x-direction using a scale factor 5
2. Rotation about z-axis 30 degree
3. Shearing in x- and y-direction with shearing factor 2 and 3, respectively.
4. Translation the point in the direction of (2,1,2)

The translation, rotation, shearing, and scaling matrices can be defined A, B, C, and D, respectively.

T=DCBA

$$A = \begin{bmatrix} 5 & 0 & 0 & 0 \\ 0 & 1 & 0 & 0 \\ 0 & 0 & 1 & 0 \\ 0 & 0 & 0 & 1 \end{bmatrix}$$

$$B = \begin{bmatrix} \sqrt{3}/2 & -1/2 & 0 & 0 \\ 1/2 & \sqrt{3}/2 & 0 & 0 \\ 0 & 0 & 1 & 0 \\ 0 & 0 & 0 & 1 \end{bmatrix}$$

$$C = \begin{bmatrix} 1 & 0 & 2 & 0 \\ 0 & 1 & 3 & 0 \\ 0 & 0 & 1 & 0 \\ 0 & 0 & 0 & 1 \end{bmatrix}$$

$$D = \begin{bmatrix} 1 & 0 & 0 & 2 \\ 0 & 1 & 0 & 1 \\ 0 & 0 & 1 & 2 \\ 0 & 0 & 0 & 1 \end{bmatrix}$$

$$T = DCBA = \begin{bmatrix} 5\sqrt{3}/2 & -1/2 & 2 & 2 \\ 5/2 & \sqrt{3}/2 & 3 & 1 \\ 0 & 0 & 1 & 2 \\ 0 & 0 & 0 & 1 \end{bmatrix}$$

Next the following cost functions are defined and described: LS, NCC, CR, and NMI. Furthermore, an overview of the literature on their use in registration for medical applications is included. Among these cost functions, the NMI-based registration has become commonplace in many medical applications [48-49].

2.4.2 Cost Function

The cost function or similarity measure evaluates the similarity between two images. In this section, the behaviors of four commonly used cost functions will be examined.

2.4.2.1 Least squares (LS)

The Least Squares (LS) method measures the average of the squared difference in image intensities [50]:

$$f = \frac{\sum_{i=1}^{N}\{R-I\}^2}{N}, \tag{2.18}$$

where R is reference image, I is input image, N is the number of values over which the sum is performed, and f is the least square. When two images differ only by Gaussian noise, the least squares will be the optimum cost function. Images of two different modalities such as MRI and PET will never differ by only Gaussian noise. Due to patient motion, even two images of the same modality, such as two MRI images, will rarely only differ by Gaussian noise. The effectiveness of LS will be extremely decreased by a small number of *voxels* having considerable intensity differences.

2.4.2.2 Correlation Ratio (CR)

The main principle of the correlation ratio (CR) method is to calculate a "similarity measure" between a reference image and an input image and search for a spatial transformation T and an intensity mapping f such that, by dis-replacing R and remapping its intensities, the resulting image f(R×T) can be seen as equivalent as possible to I. This can be obtained by minimizing the following CR function [51]:

$$\min(T, f)\, of \sum_{k} \{I(x_k) - f(R(T(x_k)))\}, \tag{2.19}$$

which integrates over the *voxel* positions in the image I. The minimum and maximum values for the CR are 0 and 1, respectively. The CR can be applied in multimodal image registration involving Positron Emission Tomography (PET), Magnetic Resonance (MR),

and Computed Tomography (CT) images, providing a good tradeoff between accuracy and robustness [52].

2.4.2.3 Normalized Cross Correlation (NCC)

The cross correlation function works very well for aligning images of the same modality. Cross correlation function is defined by the following equation:

$$CrossCorr(u, v) = \sum_{x} \sum_{y} R(x, y) I(x - u, y - v), \tag{2.20}$$

where R is reference image intensity, I is input image intensity, and x and y represent the partials of images R and I in X and Y directions, respectively. The summation is taken over the region (u, v) where R and I overlap. When I(x, y) best matches R(x, y), CrossCorr(u, v) shows the maximum value.

2.4.2.4 Normalized Mutual Information (NMI)

The algorithms of mutual information have been the most investigated measure for registration of medical image to date [53]. The mutual information of images I and J is defined by the following equation [53-54]:

$$NMI(I,J|T)=\sum_{i,j} P_{i,j}\log\frac{P_{i,j}}{p_i p_j}, \quad (2.21)$$

where $P_{i,j}$ is the joint probability distribution function of I and J, and p_i and p_j are the marginal probability distribution function of I and J, respectively. The minimum and maximum values for normalized mutual information are 0 and 1, respectively.

When images are correctly registered and aligned, there is maximal dependence between the gray values of the images, meaning that the amount of mutual information would be high. Mis-registration will cause in a decrease in the MI measure [55]. Normalized mutual information (NMI) has been used with success for a wide variety of combinations, including MR, CT, SPET, PET, and also time series images [55]. NMI can be found in a large number of studies [56-57].

2.5 Optimized Automatic Image Registration 3D

Optimized automatic image registration (OAIR) is a robust image registration algorithm developed by Woods et al. [58-61]. The OAIR technique specifies a transformation that minimizes a cost function, which represents the quality of alignment between two images. The method assesses the cost function at the number of different image resolutions, starting with the lowest resolution. Each step of increasing resolution uses the previously specified optimal transformation as the starting point and further refines its values. OAIR works very well with images of the same modality (MRI-MRI, CT-CT, PET-PET, etc.) [61]. During the OAIR registration, the re-sampling process will

influence the computed value of the cost function; therefore, choosing the best interpolation is important.

2.5.1 Outline of the OAIR method

1. The registration algorithm specifies the minimum resolution for each dimension of the target and reference images (they are subsampled by factor two, four, and eight).
2. The reference and target images are interpolated in order to create high resolution isotropic *voxels*.
3. The centers of mass (COM) for the reference and target images are then calculated and one translation level is implemented to align the COM. The method uses the right-hand convention in 3D coordinate systems (X, Y, Z) in order to compute the COM. In the image space, the left-hand corner of the image is set to (0, 0, 0). The y-axis goes top to bottom, the x-axis goes left to right, and the z-axis goes into the image. To compute the COM, the characteristics function of an object in an image is defined by the following equation:

$$b(x,y,z) = \begin{cases} 1, & \text{for points inside of the image} \\ 0, & \text{for points outside of image} \end{cases} \tag{2.22}$$

Next, the area of the image is computed as

$$S = \iiint b(x,y,z)dxdydz \tag{2.23}$$

Figure 17 shows the COM:

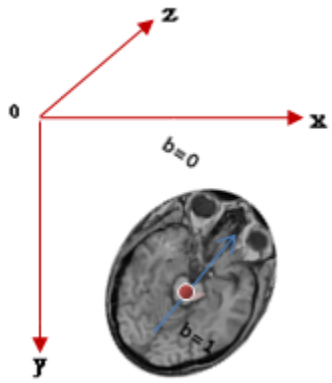

Figure 17: Calculating the COM in the image space, the left hand corner of the image is set to (0, 0, 0). The x-axis goes left to right, the y-axis goes top to bottom, and the z-axis goes into image.

The COM, indicated by $(x_{com}, y_{com,} z_{com})$ is given by the first moments of the object:

$$x_{COM} = \frac{\iiint xb(x,y,z)dxdydz}{\iiint b(x,y,z)dxdydz} \tag{2.24}$$

$$y_{COM} = \frac{\iiint yb(x,y,z)dxdydz}{\iiint b(x,y,z)dxdydz} \tag{2.25}$$

$$z_{COM} = \frac{\iiint zb(x,y,z)dxdydz}{\iiint b(x,y,z)dxdydz} \tag{2.26}$$

2.5.2 Optimization Steps

The theoretical registration problem is completely determined by an interpolation method, a cost function, and a transformation space. However, in practice, an optimization method is needed to find the transformation that minimizes the cost function [62]. In general, all cost functions require global optimization. As a part of the transformation optimization process, the images are subsampled by several factors (e.g., eight, four, and two times) [63].

Levels Eight, Four, and Two optimization: Reference and target images are interpolated and subsampled by eight, so each image is eight times smaller. The parameters corresponding to the minimum cost function is specified and used as the initial transformation. For the next level (level four) in the optimization, the reference and target images are interpolated and subsampled by four and, like in level eight, the transformation parameters corresponding to the minimum cost function are specified and used as the initial transformation for the next level (level two) in the optimization. For level two optimization, the process repeats, except that the reference and target images are first interpolated and subsampled by factor two. As mentioned above, the parameters of the transformation are systematically varied, and the cost function is assessed for each setting.

The merit of this multi-resolution technique is that initial optimization, at large n, has a noticeably reduced computational load, since the number of sample points is considerably less. Additionally, large subsampling (n=8) uses the lowest resolution image

and coarse rotation angle, in which the large features of the image is dominate, and so the overall alignment is easier to find.

3 Materials and Methods

3.1 Methodology

This work utilizes the concept of acquiring LR images that are not from the same slice planes. Figure 18 shows three scans with the same in-plane resolution but different orientations. Each LR volume is then mapped onto an HR grid based on a *priori* knowledge of the in-plane resolution. Afterwards, three HR-fitted volumes from different planes and the spacing (gaps) are combined, if present, the researcher would then apply interpolation with the flexibility to choose an appropriate interpolator to fill in the remaining gaps in the volume in a manner preserving the original HR in-plane resolution from each individual volume.

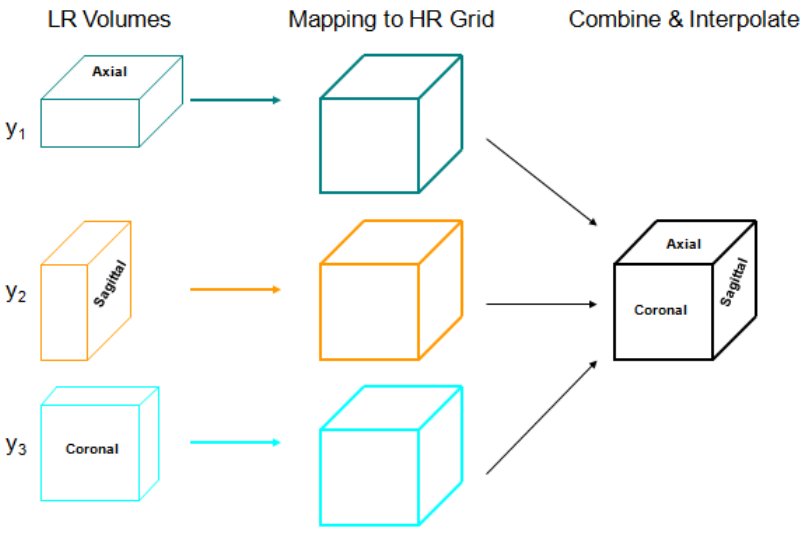

Figure 18: The proposed scheme includes three stages: (a) acquiring LR volumes, (b) mapping LR volumes to a common high resolution (HR) grid, and (c) combining and interpolating the registered LR volumes.

3.2 The Main Stages for Super Resolution

The SR image reconstruction technique consists of four main stages: up-sampling, restoration, registration, and combination. These stages can be performed separately or simultaneously. My scheme for super resolution is illustrated in Figure19.

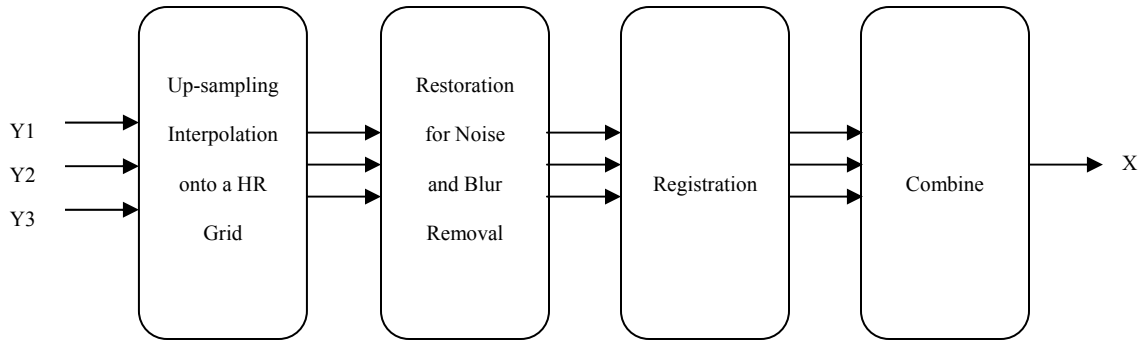

Figure 19: Scheme for super resolution. Y1, Y2, and Y3 are LR images. X is HR image.

This methodology was implemented using MATLAB (*www.mathworks.com*) and MIPAV (*www.mipav.cit.nih.gov)* for interpolation and the image registration, including the processing of images and image assessments. JMP was used to perform statistical analyses. A computer with a 2.13 GHz 2 processor was used to run MATLAB and MIPAV and to perform the image processing tasks.

3.2.1 Determining an Appropriate Interpolation

A 3D Spoiled Gradient Recalled (SPGR) MRI of the brain was acquired at Nationwide Children's Hospital of Columbus, Ohio, using a 3T GE MR scanner from a 34-year-old patient. Interpolation techniques were performed on brain scans. Relevant imaging parameters are listed in Table 1. The first initial reference image dimensions were 512*512*120 (this is native scanner output) with slice thickness of 1.3 mm (acquiring a fully isotropic 3D scan was not feasible because of time, motion artifact, and SNR factors). Because of interpolation time, I simulated the new 3D HR images (simulated Reference 2) with resolution 256*256*120 and with *voxel* size of 1mm * 1mm * 1.3mm and with slice thickness and spacing between slices of 1.3 mm.

Table 1: Imaging parameters associated with 3D reference and low-resolution images.

3D images	# of slice	Matrix size	Voxel size (mm)
Reference 1	120	512×512	0.5×0.5×1.3
Simulated Reference 2	120	256×256	1×1×1.3
Low Resolution 1	60	512×512	0.5×0.5 ×2.6
Low Resolution 2	60	256×256	1×1×2.6
Low Resolution 3	120	256×128	1×2×1.3
Low Resolution 4	120	128×256	2×2×1.3

The first LR images were generated from reference one, and the resolution was decreased (512*512*60 and with a *voxel* size of 0.5mm * 0.5mm * 2.6mm) along the slice direction by subsampling by factor of 2. The second, third, and fourth LR images were generated from simulated reference 2, and they were subsampled by factor of 2 in

the X, Y, and Z directions. The second LR images were generated with resolution 256*256*60 (axial plane) and with *voxel* size of 1mm * 1mm * 2.6mm. The third LR images were generated with resolution 256*128*120 (sagittal plane) and with *voxel* size of 1mm * 2mm * 1.3mm, and finally, the fourth LR images were generated with resolution 128*256*120 (coronal plane) and with *voxel* size of 2 mm * 1mm * 1.3mm. I rotated the LR images in x direction by 5 degrees. Then, I translated the rotated image above in x by 2 mm and in y by 3 mm. Each LR image is corrupted by Gaussian noise (10 standard deviation) and Gaussian blurring (5 radius).

Afterward, I used these LR images as input to my interpolation algorithms (trilinear, cubic Lagrangian, quintic Lagrangian, heptic Lagrangian, windowed Sinc, B-spline 3rd order, and B-Spline 4th order) to remap to a common size. They were upsampled and back to their original dimension (256*256*120), and then I compared them to the reference images in order to find the best interpolation (quantitative and qualitative assessments). Image restoration was implemented upon the upsampled images to reduce blurring and noise. Restoration can be implemented by applying any deconvolution method that considers the presence of noise.

3.2.2 Implementation of Registration Algorithm on 3D MR images

OAIR is applied on high resolution data set (Simulated reference 2) with resolution 256*256*120 and with *voxel* size of 1mm * 1mm * 1.3mm, and the

transformed image with resolution of 256*256*120 and with *voxel* size of 1mm * 1mm * 1.3mm (I repeated the same procedure for LR images 3 (sagittal plane) and LR images 4 (coronal plane). Throughout the OAIR, when an optimal fit was achieved, the target image was reformatted using the transformation function and interpolations described above to match the reference image. For achieving a good registration (intensity-based cost function) between the fixed image (reference image) and the moving image (target image), the re-sampling was essential because the moving image did not necessarily have the same origin, spacing, and number of pixels as the fixed image. Therefore, the re-sampling process helped me to have the moving image in the grid of the fixed image.

The intensity-based registration method looked for the transformation that would give the smallest value of the cost function, which I assumed was the transformation that also gave the best alignment. During this registration for analyzing the effect of interpolation and cost function, I applied and tested various interpolations and cost functions. The cost functions which are performed in this method include:

1. Normalized mutual information (NMI)
2. Normalized Cross Correlation (NCC)
3. Least Squares (LS)
4. Correlation Ratio (CR)

3.2.3 Implementation of a Super Resolution Algorithm

In my implementation of the super-resolution algorithm, I selected the best registered images with the minimum error in cost function and interpolation. I revisited my earlier hypothesis that accurate image registration and interpolation are critical in the super resolution process. As a result, the super resolution requires up-sampled images in three perspectives with the minimum error in interpolation (axial, sagittal, and coronal). Image registration was performed after the three planes were mapped onto a common space, and one volume was chosen as the fixed image (axial), and the other two as the moving images (sagittal and coronal). I determined the best cost function and interpolation during registration. Then, each registered image mapped onto an HR grid based on a *priori* knowledge of the in-plane resolution. Afterwards, I combined three HR fitted volumes from different planes and the spacing (gaps), if present, I then applied interpolation to fill in the remaining gaps in the volume in a manner preserving the original HR in-plane resolution from each individual volume.

3.3 Image Assessment

There are various ways to evaluate the accuracy of interpolation techniques, registration, and SRR. They can be divided into qualitative and quantitative methods. For qualitative and quantitative assessment of registered images, I proposed five ways to

compare and evaluate the new transformation with the old; I needed to quantify the deference between the geometrically transformed source images with the target image.

3.3.1 Quantitative Assessment

For the quantitative assessment, I considered a mean square error (MSE), peak signal-to-noise ratio (PSNR), entropy, and statistical analyses of images including average *voxel* intensity, standard deviation of intensity, median intensity, mode intensity, coefficient of skewness, and coefficient of kurtosis. The MSE and PSNR measures are estimates of the quality of interpolation and registration images and entropy is also suitable choice for quantitative assessment the accuracy of registration method.

3.3.1.1 Mean Square Error

MSE was computed between the original image (reference) and registered image in order to measure the average of the squared difference in image intensities:

$$SE_{ijk} = (R(p_{ijk}) - I(p_{ijk}))^2, \tag{3.1}$$

where I, j, k represent the direct comparison of each coordinate location and $R(p_{ijk})$ is the reference image(minimum reference image value (p_{ijk})) and $I(p_{ijk})$ is input image(p_{ijk})

(minimum input image value (p_{ijk})). The MSE was computed for 3D brain image in order to assign a value and compare the results.

$$\mathrm{MSE} = \frac{\sum_{i=1}^{n}\sum_{j=1}^{m}\sum_{k=1}^{l} \mathrm{SE}_{ijk}}{\mathrm{n.m.l}}, \tag{3.2}$$

here n, m, l are the number of points in the x, y, z directions, respectively, for the reconstructed volume.

3.3.1.2 Peak signal to noise

The PSNR in decibels (dB) between the original image and the registered image is defined by [64],

$$PSNR = 20 \times \log_{10}\left(\frac{MAX}{RMSE}\right), \tag{3.3}$$

where MAX is the maximum pixel value of the image and RMSE is the square root of the MSE.

3.3.1.3 Entropy

The desire for a measure of information (commonly termed *entropy*) of a message stems from communication theory [65]. Shannon introduced an adapted measure in 1984

[66], which weights the information per outcome by the probability of that outcome occurring. Given events occurring with probabilities, the Shannon entropy is defined as

$$H=\sum_i p_i log \frac{1}{p_i}=-\sum_i p_i log p_i \ , \tag{3.4}$$

where p= (histogram count in bin)/total count. The Shannon entropy is not only restricted to the probabilities of letters or words, but can be applied and computed for an image and be used on the distribution of the gray values of the image. An image with a low entropy value has almost a single intensity; it contains very little information. An image with a high entropy value has more or less equal quantities of numerous different intensities; it contains a lot of information [65]. For instance, blurring images reduces noise and high frequency and thus sharpens the images histogram, resulting in reduced entropy.

3.3.1.4 Statistical analyses

A primary task in many statistical analyses is to specify variability of a data set. A further characterization of the data contains skewness and kurtosis. The histogram is a great graphical technique for showing both the kurtosis and skewness, and these numerical measures of shape give a more precise evaluation.

Skewness is a measure of symmetry, or more precisely, the lack of symmetry. If the greater part of the data is at the right and the left tail is longer, one could say that the distribution is negatively skewed or skewed left. If the peak is toward the left and the

right tail is longer, one can conclude that the distribution is positively and skewed right [37-38].

The skewness is defined as equation [37],

$$\text{Skewness} = \frac{\sum_{i=1}^{N}(Y_i - \bar{Y})^3}{(N-1)s^3}, \tag{3.5}$$

where $\bar{Y}$ is the mean N is the number of data points, and s is the standard deviation. The skewness for symmetric data is close to zero and for normal distribution is zero.

Kurtosis is a measure of whether the data are sharp (peaked) and high or flat and short relative to a normal distribution. Higher values show a sharper, higher peak; lower values show a lower, shorter peak.

The kurtosis is defined as equation [38],

$$\text{Kurtosis} = \frac{\sum_{i=1}^{N}(Y_i - \bar{Y})^4}{(N-1)s^4}, \tag{3.6}$$

where $\bar{Y}$ is the mean, N is the number of data points, and s is the standard deviation. The kurtosis for a standard normal distribution is three, and some sources use the different format for definition of kurtosis (usually called "excess kurtosis")[38]:

$$\text{Kurtosis} = \frac{\sum_{i=1}^{N}(Y_i - \bar{Y})^4}{(N-1)s^4} - 3, \tag{3.7}$$

with the second definition of kurtosis, the standard normal distribution has a kurtosis of zero. Moreover, with Equation 3.7, positive kurtosis displays a "peak" distribution and negative kurtosis displays a "flat" distribution.

Tukey's Honestly Significant Difference (HSD) Test

The main purpose of the HSD is to compute the honestly significant difference (i.e., the HSD) between two means using a statistical distribution defined by Student and called the q distribution. The q statistics evaluating the difference between groups x and $x^{-}$is defined as equation [67],

$$q = \frac{M_x - M_{x^-}}{\sqrt{\frac{1}{2} MS_{s(A)} (\frac{1}{S_x} + \frac{1}{S_{x^-}})}}, \tag{3.8}$$

where the number of observations of the x-th group is denoted S_x, M_x is the mean of group x, M_{x^-} is the mean of group x^{-}. The mean square of error is denoted $MS_{s(A)}$. Rewriting equation 3.8 illustrates that a difference between the means of group x and x^{-}will be significant if

$$|M_x - M_{x^-}| > HSD = q\sqrt{\frac{1}{2} MS_{s(A)} (\frac{1}{S_x} + \frac{1}{S_{x^-}})} \tag{3.9}$$

We take the absolute value of the difference between the means and compare it to the value of HSD in order to assess the difference between the means of group x and x^{-}, if

$$|M_x - M_{x^-}| \geq HSD, \tag{3.10}$$

then the comparison is shown significant at the selected $\boldsymbol{\alpha}$-level (usually 0.05 or 0.01).

3.3.2 Qualitative Assessment

One way for qualitative assessment is the subtraction of the reference and registered images. Image subtraction techniques can be used to detect subtle changes that may reflect clinically important disease progression [41]. Another way to conduct a qualitative assessment is to create a joint histogram. The joint histogram is a functional tool for visualizing the relationship between the intensities of corresponding *voxels* in two or more images. Visual assessment is also considered for qualitative assessment.

3.3.2.1 Joint Histogram

The joint histogram is two-dimensional for two grayscale images A and B and is created by plotting the intensity of each *voxel* in image A against the intensity of the corresponding *voxel* in image B. When two images of different modalities are produced, the spatial resolution is likely to be different (see Figure 20). Therefore, before

calculating a joint histogram, it is essential to rescale the range of data of the first image to the range of data of the second image.

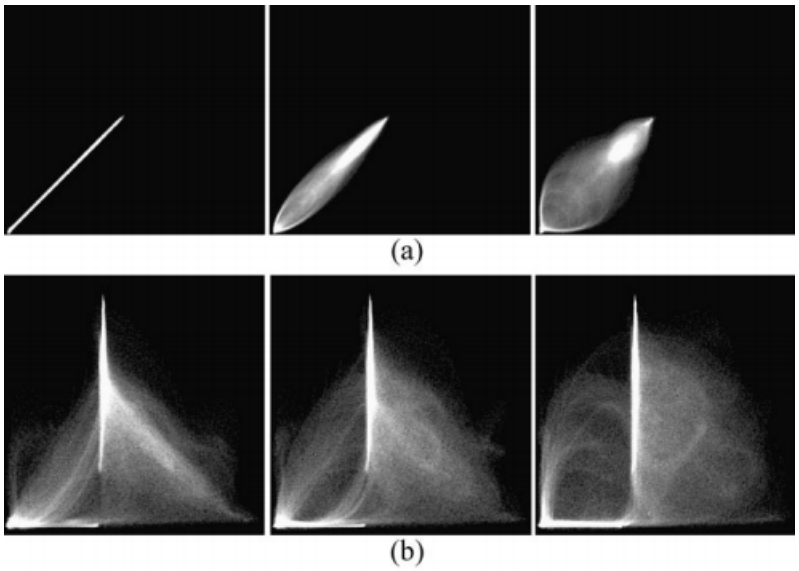

Figure 20: Example 2D histograms for (a) the same MR images of the head, (b) MR and CT images of the head. The left column shows two images when aligned, the middle column shows two image when translated by 2 mm, and the right column when translated by 5 mm. As can be seen, the joint histogram disperses with increasing mis-registration (obtained from Hill et al. (1994)).

When two images are perfectly aligned, the corresponding anatomical areas overlap, and their joint histogram is highly focused. In misaligned images, anatomical areas are not matched, and they are mixed up and their joint histogram is scattered. For example, images of the cerebrum over the skull cause a more dispersed joint histogram. Example joint histograms for different modalities like MR–CT and PET–MR at different stages are investigated in some papers [68-69]. I implemented the joint histogram

technique on the registered images for checking the effect of interpolations and cost functions on the accuracy of OAIR.

4 Results and Discussion

4.1 Evaluating Interpolation Techniques on 3D MR Images

In Figure 21, the interpolated images in axial, coronal, and sagittal views are shown for the first LR images. Part (a) illustrates the 3D image interpolated by the trilinear method in part (b), the image generated by a heptic Lagrangian and quintinc Lagrangian interpolation images appear in part (c). Part (d), part (e), and part (f) show 3D images are generated by windowed Sinc, cubic Lagrangian, and nearest neighbor interpolation, respectively. The B-spline 3rd and B-spline 4th interpolations are shown in parts (g) and (h), respectively.

Average *voxel* intensity, standard deviation of intensity, median intensity, mode intensity, coefficient skewness, and coefficient of kurtosis for trilinear, nearest neighbor, B-Spline 3rd, B-spline 4th, cubic Lagrangian, quintic Lagrangian, heptic Lagrangian, and windowed Sinc interpolations are calculated and presented in Table 2.

Statistical analysis of interpolated images shows the effect of various interpolations on the brain images. For instance, when comparing the skewness of the interpolated dataset and the skewness of original dataset, one can figure out the degree of deviation of the interpolated dataset from original dataset and find which interpolation has the least and the greatest effect on deviation of the dataset. The kurtosis is a measure of the peakedness of distribution and, like skewness, is only meaningful when compared

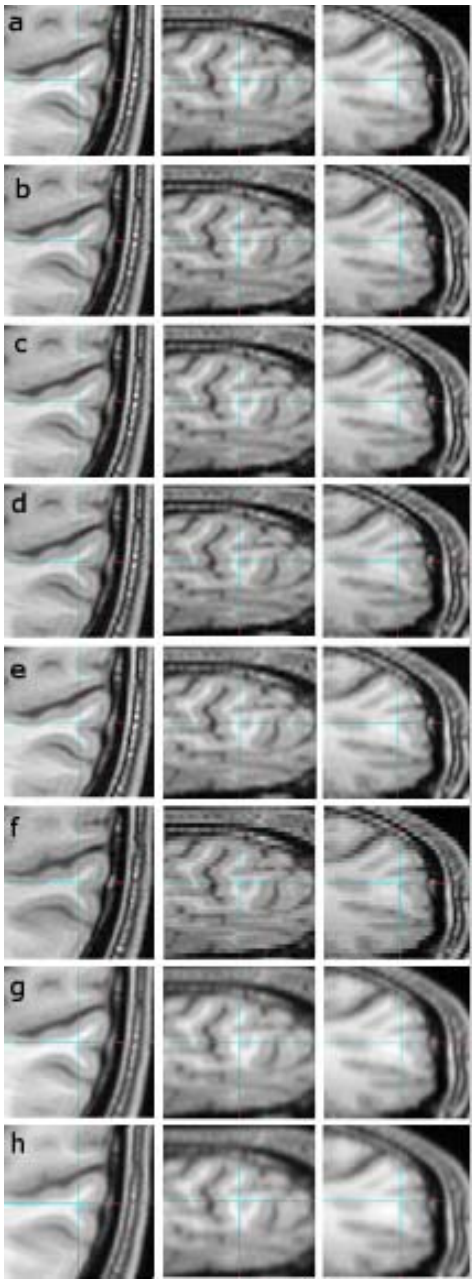

Figure 21: (a) trilinear, (b) heptic Lagrange, (c) quintinc Lagrange, (d) windowed Sinc, (e) cubic Lagrangian, (f) nearest neighbor, (g) B-spline 3rd, (h) B-spline 4th, axial view (left column), sagittal view (middle column), and coronal view (right colum). These upsampled images from images that were downsampled by factor of two in z direction.

to the kurtosis of the original image. The distribution of local contrast for this set of images has positive kurtosis. The 3D MSE for 512-sized MRI images were computed in all three planes. To further test the interpolations in 3D, three typical matrix sizes were simulated, namely 64, 128 and 256. The 3D MSE of these matrix sizes are tabulated in Table 3. The MSE is inversely proportional to the MRI images 3D size. As a result, trilinear method yields more accurate (lower MSE) results than discussed interpolations.

Table 2: Statistical analysis for high resolution (HR) 3D images (reference image) with resolution 512*512*120 and upsampled 3D images (low resolution (LR)) with resolution 512*512*120 for different interpolations.

Type of image	Interpolation	Avg voxel Intensity	Std Dev of intensity	Median Intensity	Mode intensity	Coefficient of Skewness	Coefficient of Kurtosis
HR	_____	2910.9122	1132.3098	3201	3947	-0.7769	2.7526
LR	Trilinear	2924.9699	1054.8091	3185	3132	-0.8241	2.8657
LR	Nearest Neighbor	2900.7527	1110.7623	3186	4127	-0.7638	2.6874
LR	Bspline 3rd	2926.8911	1027.1978	3175	3837	-0.8231	2.9146
LR	Bspline 4th	2882.9325	1047.9794	3139	3522	-0.7561	2.7124
LR	Cubic Lagrangian	2936.4279	1082.3182	3206	3925	-0.8375	2.8915
LR	Quintic Lagrangian	2908.1333	1104.319	3188	3935	-0.8011	2.7711
LR	Heptic Lagrangian	2931.6694	1090.0487	3203	3110	-0.8236	2.8568
LR	Windowed Sinc	2964.7134	1109.5314	3242	3587	-0.8138	2.8282

Table 3: 3D MSE for MR images of 64-512 for interpolations of trilinear, nearest neighbor, B-spline 3rd, B-spline 4th, cubic Lagrangian, quintic Lagrangian, heptic Lagrangian, windowed Sinc.

	MSE			
Interpolation	64	128	256	512
Trilinear	0.22683	0.03088	0.00282	0.00024
Nearest Neighbor	0.75852	0.09615	0.01295	0.00135
Bspline 3rd	0.50714	0.06435	0.00706	0.00095
Bspline4th	0.32088	0.05742	0.00618	0.00075
Cubic Lagrangian	0.24283	0.04956	0.00554	0.00027
Quintic Lagrangian	0.24204	0.03286	0.00552	0.00026
Heptic Lagrangian	0.24181	0.03284	0.00549	0.00025
Windowed Sinc	0.24338	0.05123	0.00559	0.00027

Also, the interpolated images were quantitatively evaluated by computing the PSNR, which is widely utilized in the evaluation of reconstructed images [28]. The 3D PSNR for 64-512 sized MRI images were computed. The 3D PSNR of these matrix sizes are tabulated in Table 4. The PSNR results for trilinear interpolation for matrix size of 64-512 were approximately 91 (dB), 100 (dB), 111 (dB), and 121 (dB), respectively. Based on the Table 4, trilinear interpolation shows PSNR superiority against the other interpolation. In addition, the PSNR was found to slowly increase as the matrix size increased.

The second LR images, the matrix size of 256*256*60 (axial view), the third LR images, the matrix size of 256*128*120 (sagittal view), and the fourth LR images, the matrix size of 128*256*120 (coronal view) were simply interpolated separately and MSE computed. The results are tabulated in Table 5.

Table 4: 3D PSNR for MR images of 64-512 for interpolations of trilinear, nearest neighbor, B-spline 3rd, B-spline 4th, cubic Lagrangian, quintic Lagrangian, heptic Lagrangian, windowed Sinc.

	PSNR (dB)			
Interpolation	64	128	256	512
Trilinear	91.95	100.61	111.01	121.76
Nearest Neighbor	86.78	95.76	104.47	114.29
Bspline 3rd	87.62	96.57	106.17	114.73
Bspline4th	89.44	96.92	106.60	115.93
Cubic Lagrangian	91.73	98.63	108.14	121.29
Quintic Lagrangian	91.74	100.42	108.16	121.45
Heptic Lagrangian	91.75	100.44	108.19	121.61
Windowed Sinc	91.72	98.49	108.11	121.28

As a result, in Table 5, the interpolated matrix size of 256*256*60 (axial view) yields more accurate (lower MSE) results than both matrix sizes of 256*128*120 (sagittal view), 128*256*120 (coronal view). In other words, the interpolated images in z direction have more quality (lower MSE) than the interpolated images in x and y directions. However, the perceived quality of 128*256*120 (coronal view) was nearly as good as that of 256*128*120 (sagittal view). Full listings of statistical analysis for interpolations can be found in the Appendix A.

Table 5: 3D MSE for MR image of matrix sizes of 256*256*60, 256*128*120, and 128*256*120 for interpolations of trilinear, nearest neighbor, B-spline 3rd, B-spline 4th, cubic Lagrangian, quintic Lagrangian, heptic Lagrangian, windowed Sinc (compared to 3D simulated reference 2 with resolution 256*256*120).

	MSE		
Interpolation	256×256×60	256×128×120	128×256×120
Trilinear	0.002793	0.002820	0.002983
Nearest Neighbor	0.014754	0.016352	0.016544
Bspline 3rd	0.010866	0.013058	0.012870
Bspline 4th	0.006383	0.007063	0.007319
Cubic Lagrange	0.004519	0.005546	0.005213
Quintic Lagrange	0.004504	0.005530	0.005195
Heptic Lagrange	0.004132	0.005524	0.005192
Windowed Sinc	0.004605	0.005660	0.005285

4.1.1 Visual Quality of Interpolation Techniques

In Figure 22, I applied the trilinear algorithm on the second LR images, and the resolution in the axial view did not improve because the resolution in x and y directions were already high (256*256*60) with *voxel* size of 1mm * 1mm * 2.6mm, and resolution in axial direction was constant. In contrast, the resolutions in sagittal and coronal views showed different results, and I saw enough improvement in both planes (interpolated images). As was mentioned before, the resolution in the slice-selection direction is lower than plane direction, and I would like to improve the resolution in the slice-selection direction. In Figure 23, I applied a trilinear algorithm on the third LR images with resolution 256*128*120 and *voxel* size of 1mm * 2mm * 1.3mm, the resolution in coronal view did not improve because the resolution in x-direction was high. However, the resolutions in sagittal and axial views were changed, and I saw enough improvement in their resolutions. The fourth LR images had a resolution of 128*256*120 and *voxel*

size of 2mm * 1mm * 1.3mm; those results are shown in Figure 24. The resolution in sagittal view was constant because the resolution in Y was high and just the sagittal resolution in axial and coronal views were changed. The downsampled results in Figure 22 (middle row) sagittal and coronal views show significant jaggy edge distortion. The trilinear interpolation results in Figure 22 (bottom row) and coronal views have smoother edges but somewhat blurred appearance overall. Also, the downsampled results in Figure 23 (middle row) axial and sagittal views are almost equivalent to downsampled results in sagittal and coronal views in Figure 22, and they show noticeable jagged-edge distortion. The trilinear interpolation results in Figure 23 (bottom row) axial and sagittal views have smoother edges, but blurred appearance slightly. One can see enough improvement in resolution of both planes (axial and sagittal), but the resolution of the coronal view is constant. The downsampled results in Figure 24 (middle row) are similar to the downsampled results in Figures 22 and 23, but with different perspective (axial and coronal). The trilinear interpolation results in Figure 24 (bottom row) axial and coronal views show enough improvement in their planes, but the sagittal view is constant.

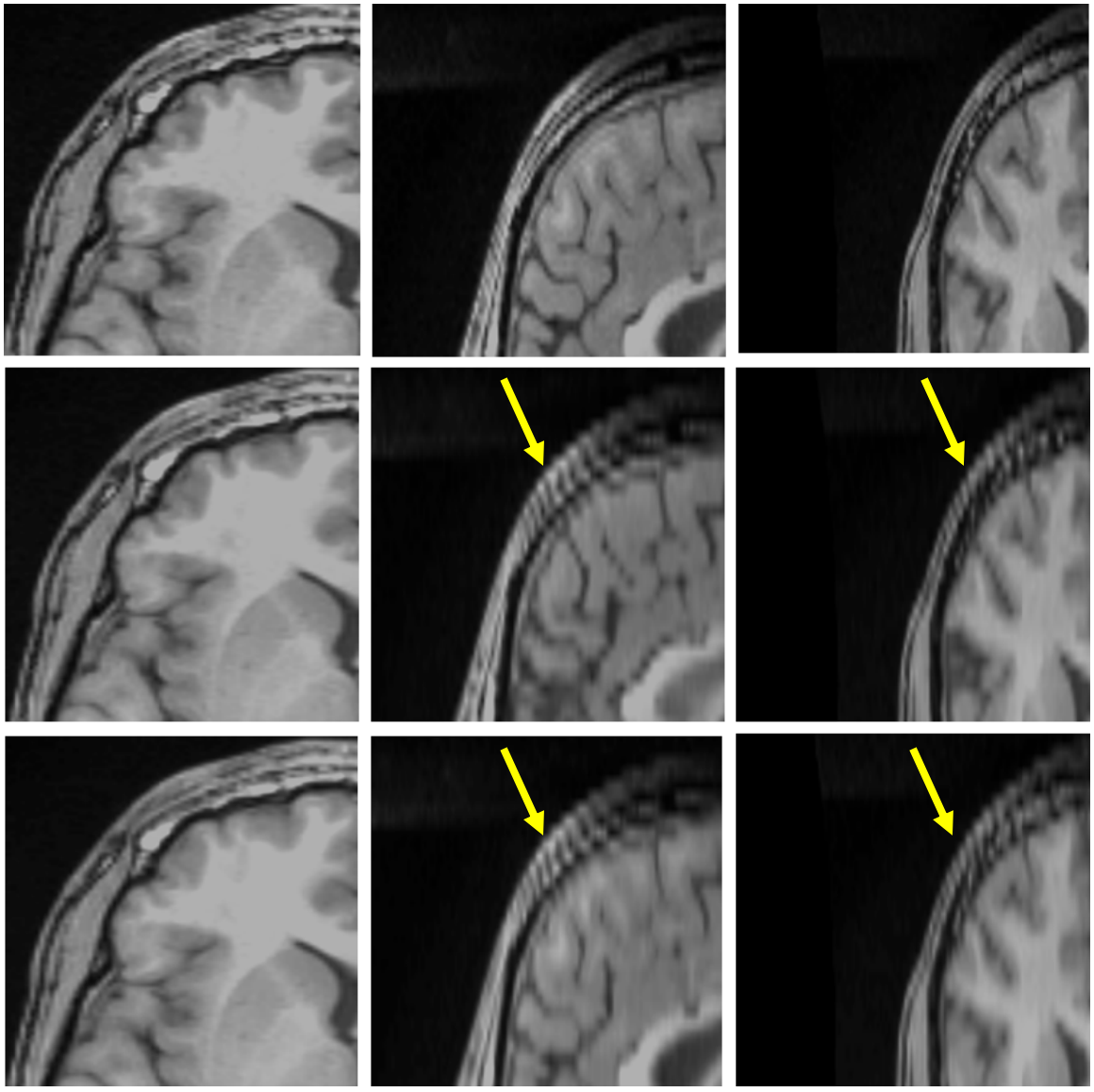

Figure 22: Reference with resolution 256*256*120 (top row), Downsampled by a factor of 2 in the Z direction with resolution 256*256*60 (middle row), interpolated by trilinear (bottom row), axial view (left column), sagittal (middle-column), coronal view (right column). The Yellow arrows in sagittal and coronal views show significant jaggy edge distortion.

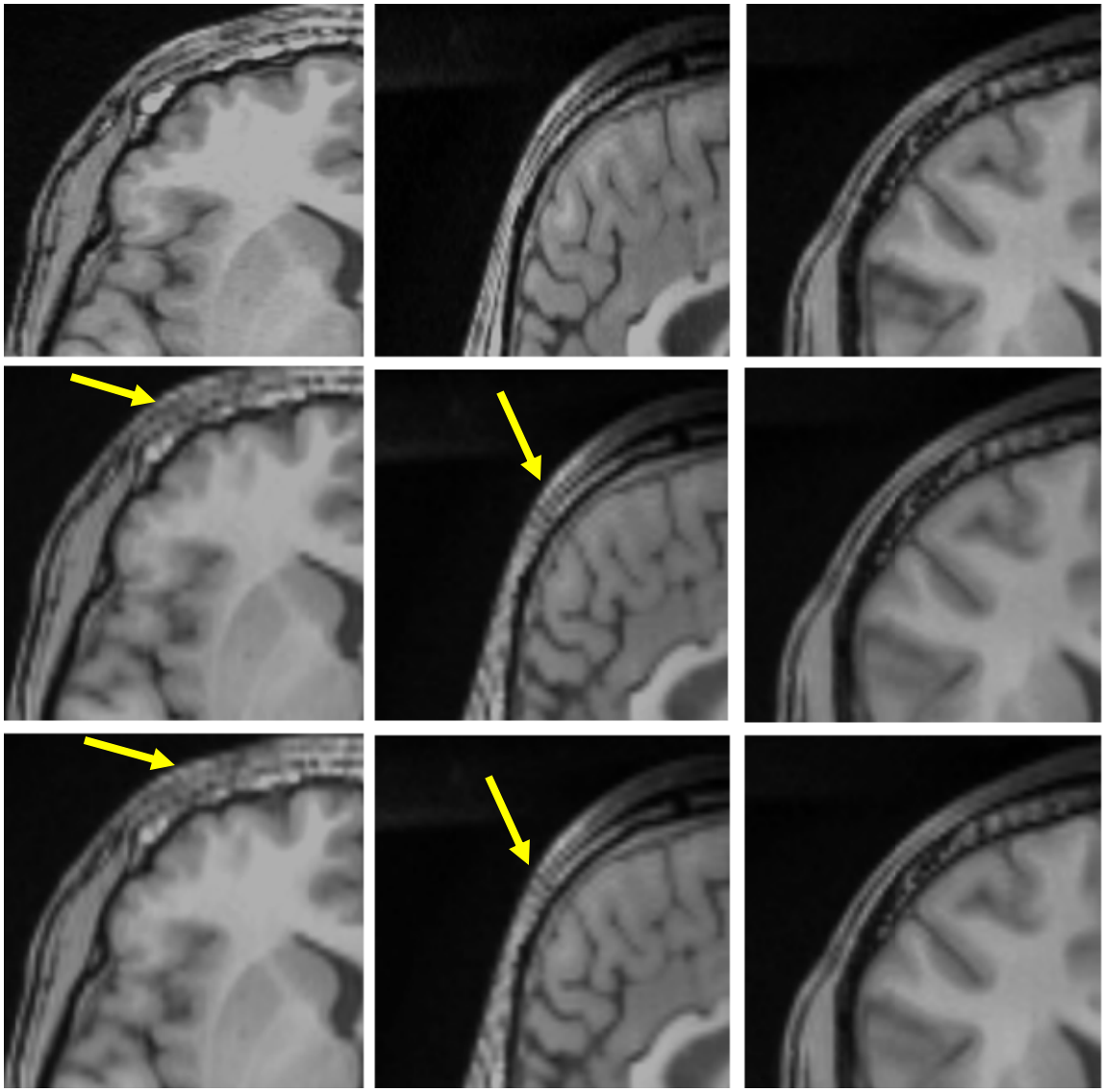

Figure 23: Reference with resolution 256*256*120 (top row), downsampled by a factor of 2 in the Y direction with resolution 256*128*120 (middle row), interpolated by trilinear (bottom row), axial view (left column), sagittal (middle column), coronal view (right column). The Yellow arrows in axial and sagittal views show significant jaggy edge distortion.

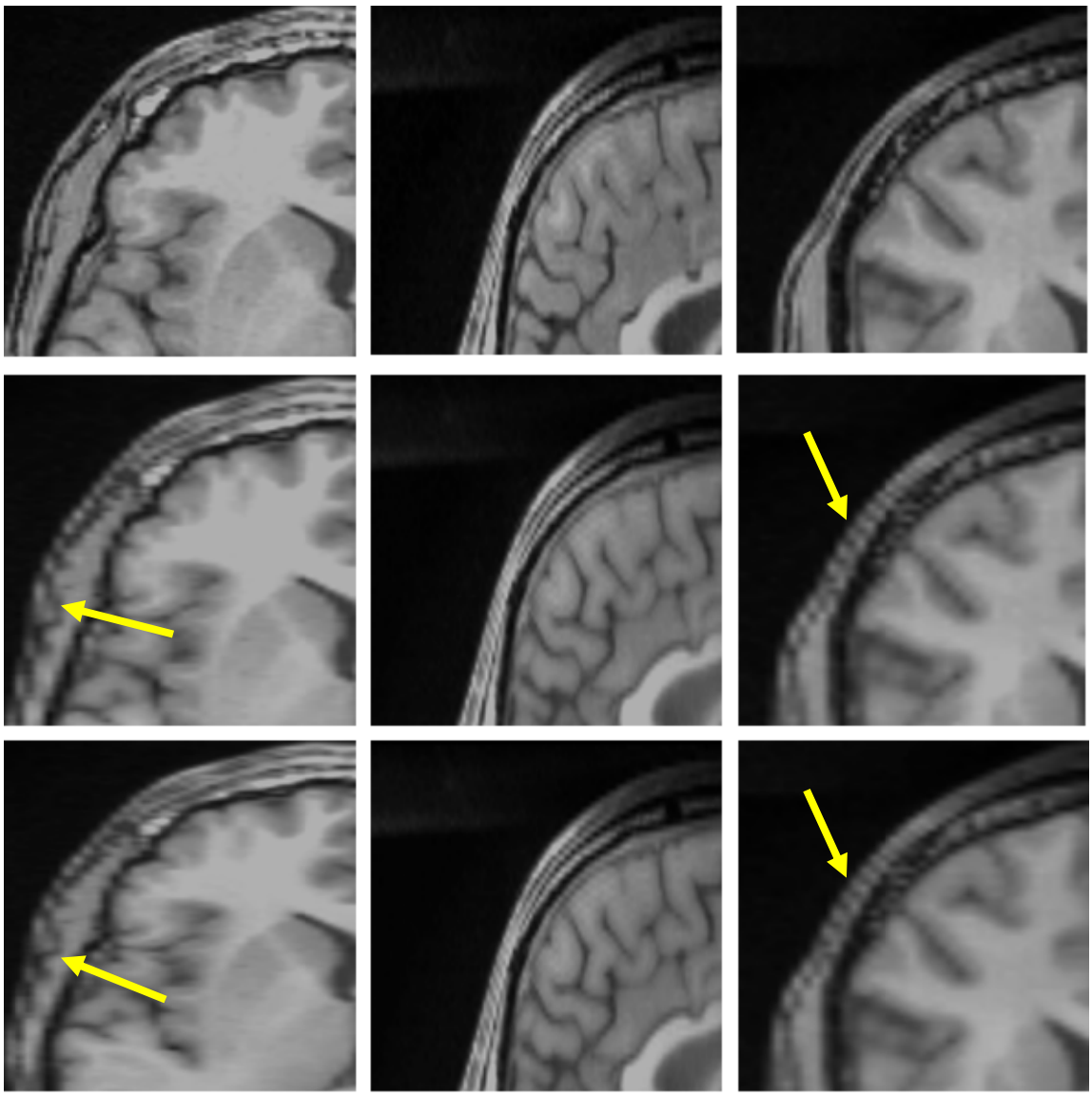

Figure 24: Reference with resolution 256*256*120 (top row), downsampled by a factor of 2 in the X direction with resolution 128*256*120 (middle row), interpolated by trilinear (bottom row), axial view (left column), sagittal (middle column), coronal view (right column). The Yellow arrows in axial and coronal views show significant jaggy edge distortion.

4.1.2 Runtime Measurement

The runtimes of the various interpolation schemes were computed on MR images with resolution 256*256*60(axial view). In the axial view, the nearest neighbor is the fastest interpolation and runs quickly, with 16.8 s, and trilinear is a bit slower than the nearest neighbor and runs with 20.4 s. Cubic Lagrangian is fairly fast and requires less time (35.7 s) than the quintic Lagrangian, heptic Lagrangian, and windowed Sinc, with 75.2, 159.6 and 182.3, respectively. Interpolation with the B-spline 3rd and B-spline 4th took about 48 and 185 times as long as nearest neighbor interpolation. This weak performance is caused by evaluation of the exponential function necessary to specify the weights and increasing the order of B-spline slows the interpolation rapidly. The results of the run times are presented in Figure 25.

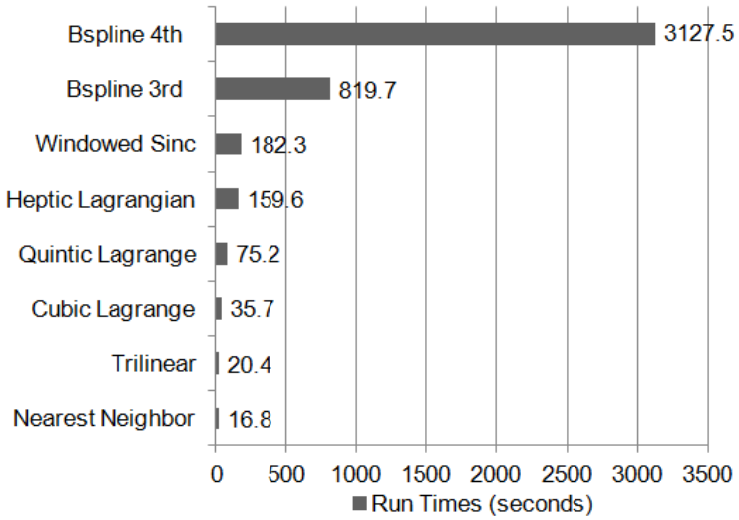

Figure 25: Run times measured on the Intel Xeon with 2.13 GHz 2 processor. Among the discussed interpolation techniques, the trilinear is one of the fastest interpolations and runs quickly, with 20.4 s.

Among the interpolations techniques discussed, the trilinear method is one of the fastest techniques and has the smallest interpolation error. Nearest neighbor has a strong point that the original *voxel* intensities are preserved, but the resulting image is degraded significantly and has a blocky appearance. My experiments show the heptic Lagrangian technique to have smaller error than the quintic Lagragian and the cubic Lagragian. The windowed Sinc has smaller error than the nearest neighbor, B-spline 3^{rd}, B-spline 4^{th}. The main drawback of windowed Sinc interpolation is that in aliased image, it generates significant ripple artifacts in the surrounding of image edges. The B-spline 3^{rd}, B-spline 4^{th} are the slowest techniques in this study, and B-spline 3^{th} produces one of the worst results in terms of similarity to the original image, and of the bottom method. My results demonstrated increment of the order in B-spline will not significantly improve the interpolation quality, and this will just magnify the edge effects and the degree of blurriness, which already are noticeable when compared to trilinear and Lagrangian methods. The theory and application of B-spline are analyzed by Aldroubi, Unser, and Eden [70-72], and they found the third order B-spline interpolator to be sufficient for some specific practical applications [73]. Currently, we believe trilinear to offer the best compromise between speed and accuracy in upsampling.

4.2 Analyzing the Effect of Interpolation Techniques on Accuracy of Cost Functions Based OAIR Algorithm

I implemented OAIR 3D described in chapter 2 to perform registration between images, and eight interpolation techniques using similarity measures NCC, LS, CR, and NMI were tested. I computed MSE and PSNR of our results, and the experimental results are listed in Table 6. It is important to note that the interpolation error during upsampling (before registration) is different than the interpolation error of geometric transformation (during registration). For instance, the interpolation algorithm, which has remarkable performance in upsampling process, may have insufficient performance in geometric transformation [74]. Statistical analysis of Table 6 in Appendix A showed that there was insignificant difference between the sets of image registered using CR, LS, NCC, and NMI. But, the effect of interpolation was considerable, and I observed significant difference between the set of image registered using different interpolations. For instance, sets of images registered using windowed Sinc interpolation were significantly better than sets of image registered using B-spline 3rd interpolation with similar cost functions (lower MSE and higher PSNR). For qualitative assessment, I investigated the accuracy of registered results using intensity-based cost functions (CR, LS, NCC, NMI). Windowed Sinc and B-Spline 3rd interpolations were used during registration (other interpolations scheme can also be used if more investigation is desired.). The Figure 26 shows axial slices from two registered 3D MRI volumes with their subtractions. The panels show axial slices from two data sets (3D simulated images with resolution 256*256*120 and

Table 6*:* The 3D MSE and PSNR for registered image of 256*256*120 using interpolations of trilinear, B-spline 3rd , B-spline 4th, cubic Lagr ange, quintic Lagrange, heptic Lagrangian, windowed Sinc, and cost functions of CR, LS, NCC, and NMI. The Affine Transformation contains 12 degrees of freedom (DOF) and was implemented during registration.

Interpolation	Cost Function	MSE	PSNR(dB)
Trilinear	Correlation ratio	0.023505	115.32
Trilinear	Least squares	0.023591	115.16
Trilinear	Normalized cross correlation	0.023597	115.10
Trilinear	Normalized mutual information	0.023623	115.09
Bspline 3rd	Correlation ratio	0.065592	106.30
Bspline 3rd	Least squares	0.065732	106.27
Bspline 3rd	Normalized cross correlation	0.064311	106.34
Bspline 3rd	Normalized mutual information	0.065588	106.31
Bspline 4th	Correlation ratio	0.037540	111.37
Bspline 4th	Least squares	0.037597	111.36
Bspline 4th	Normalized cross correlation	0.037631	111.35
Bspline 4th	Normalized mutual information	0.037604	111.36
Cubic Lagrange	Correlation ratio	0.020723	116.35
Cubic Lagrange	Least squares	0.020887	116.28
Cubic Lagrange	Normalized cross correlation	0.020891	116.27
Cubic Lagrange	Normalized mutual information	0.020793	116.32
Quintic Lagrange	Correlation ratio	0.019982	116.76
Quintic Lagrange	Least squares	0.020108	116.71
Quintic Lagrange	Normalized cross correlation	0.020082	116.72
Quintic Lagrange	Normalized mutual information	0.019979	116.76
Heptic Lagrange	Correlation ratio	0.019588	116.86
Heptic Lagrange	Least squares	0.019770	116.78
Heptic Lagrange	Normalized cross correlation	0.019736	116.79
Heptic Lagrange	Normalized mutual information	0.019639	116.83
Windowed Sinc	Correlation ratio	0.019119	117.06
Windowed Sinc	Least squares	0.019190	117.02
Windowed Sinc	Normalized cross correlation	0.019329	116.96
Windowed Sinc	Normalized mutual information	0.019160	117.04

with *voxel* size of 1mm * 1mm * 1.3mm) after registration of the three dimensional volumes using an intensity-based CR (first column), LS (second column), NCC (third column), NMI (fourth column). Windowed Sinc (top panel) and B-spline 3rd (bottom

panel) interpolations were used as re-sampling. In the second row of the panels, after registration, the pixel intensities of the reference and target images were roughly identical and different images were considerably smooth. In both panels, although differences of registered 3D MRI volumes using an intensity-based CR (first column), LS (second column), NCC (third column), NMI (fourth column) are difficult to see by eye, changing the interpolation shows that significant differences between two panels exists.

In the bottom panel, where B-spline 3rd was used during registration, the boundary of the skull, which was masked out of the images during registration, can still be observed easily in the difference images. Whereas in the top panel, where windowed Sinc was used during registration, the skull in different images are not easily detected by eye. A possible reason for checking the effect of interpolations and cost functions for registration can be seen by visual inspection of the joint histogram in Figure 27, which contains several histograms of 3D MRI using an intensity-based CR (first column), LS (second column), NCC (third column), and NMI (fourth column). In the top and bottom rows, windowed Sinc and B-spline 3rd interpolations were used during registration, respectively. The top row in Figure 27 showed the joint histogram for 3D images at registration using windowed interpolation and with small amount of mis-registration, and there is a diagonal in the distribution with the small dispersion. However, in the bottom row, the B- Spline 3rd interpolation led to large mis-registration of the image and increased off-diagonal entries started to appear, and the distribution became more

dispersed. The distribution of the bottom row is non-symmetric, and so the linear relationship is not preserved.

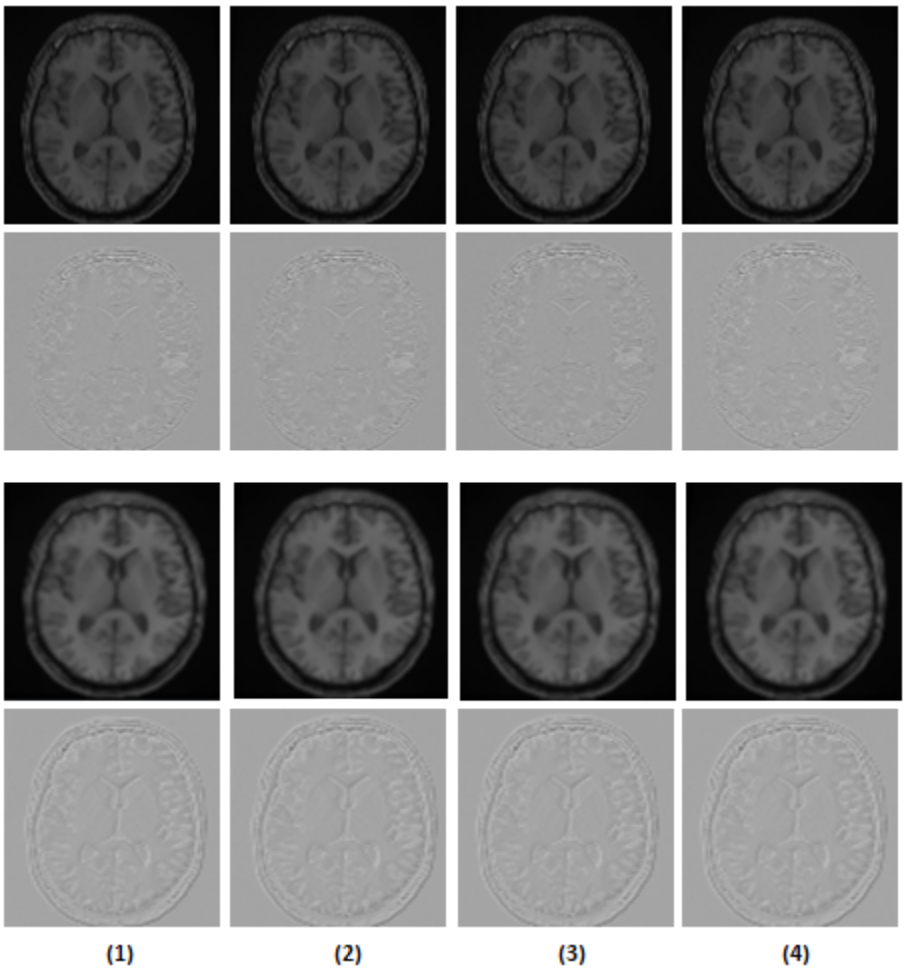

Figure 26: In the top panel, axial slices from two unregistered 3D MRI volumes using an intensity-based cost function (CR first column), LS (second column), NCC (third column), NMI (fourth column)) are shown. Windowed Sinc interpolation was used during registration for the first panel. The second row of the top panel shows subtraction of the images. The bottom panel shows similar axial slices from the same two data sets after registration of the full 3D volumes using the same intensity-based cost function (CR (first column), LS (second column), NCC (third column), NMI (fourth column)). B-spline 3rd interpolation was used during registration for the second panel. The second row of the bottom panel shows subtraction of the images. Although differences of the first row of the top and bottom panels are not easily observed by eye, subtraction of the images shows that differences are present, as seen on the second row of the top and bottom panels.

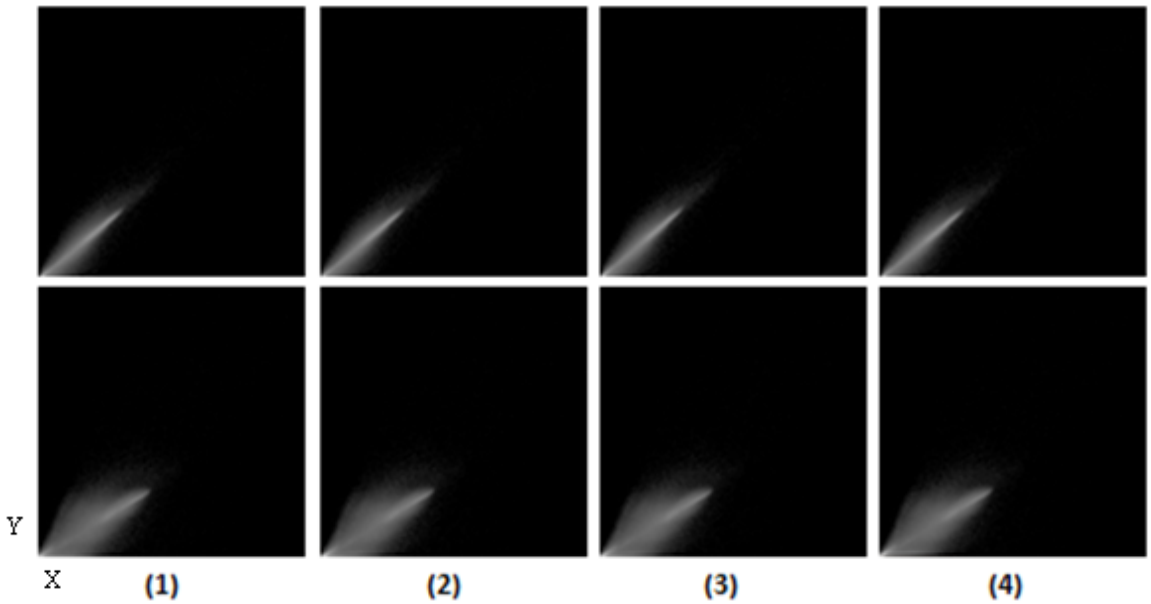

Figure 27: Joint histogram of voxel intensities for registered 3D MRI volumes using an intensity-based cost function (CR (first column), LS (second column), NCC (third column), NMI (fourth column)) are shown. The top row is generated from the images when registered using Windowed Sinc interpolation, and the bottom row is generated from the images when registered using B-spline 3rd interpolation.

In general, the intense inhomogeneity will noticeably change for different interpolations; this is one of the reasons that will induce non-symmetric dispersion and a nonlinear relationship between intensities. But, the change in the appearance of the histograms for these 3D MRI volumes using CR, LS, NCC, and NMI are *insignificant*, as shown in Appendix A. I used these joint histograms to better understand the effect of different interpolations and cost functions during registration. I also measured joint entropy of the registered images using various interpolations and cost functions. Because joint entropy is directly related, the joint probability distribution describes the statistical relationship of corresponding *voxel* intensities. Entropy increases with increasing mis-

registration as can be seen in visual appearance of the joint histogram (see Figure 27). High dispersion of the joint histogram is equivalent to high joint entropy [75]. The joint entropy results are shown in Table 7, and there are no significant differences between the entropies of registered images using CR, LS, NCC, and NMI, which means they have the similar dispersion in the joint histogram, but there are significant differences between the entropies of registered images using different interpolations. Also, I computed costs for different *voxel* similarity cost functions that were used in registration with different interpolations and cost functions. I used inverse cost functions, thus the minimum cost function corresponds to better registration. The results are shown in Table 8, and the registered images using CR, LS, NCCI, and NMI yielded very close results, whereas the registered images using different interpolations yielded different results. Statistical analysis of Tables 6, 7, and 8 in Appendix A showed that interpolations had a *significant* effect on the registration accuracy, whereas cost functions had no effect on the registration accuracy.

Table 7: The Joint entropy for the registered images of matrix size of 256*256*120 using interpolations of trilinear, B-spline 3rd, B-spline 4th, cubic Lagrange, quintic Lagrange, heptic Lagrange, windowed Sinc and cost functions of CR, LS, NCC, and NMI. Their entropies were achieved using mutual information.

Interpolation	Cost Function	Entropy
Trilinear	Correlation ratio	2.3723
Trilinear	Least squares	2.3718
Trilinear	Normalized cross correlation	2.3704
Trilinear	Normalized mutual information	2.3787
Bspline 3rd	Correlation ratio	2.4499
Bspline 3rd	Least squares	2.4486
Bspline 3rd	Normalized cross correlation	2.4489
Bspline 3rd	Normalized mutual information	2.4529
Bspline 4th	Correlation ratio	2.3874
Bspline 4th	Least squares	2.3889
Bspline 4th	Normalized cross correlation	2.3891
Bspline 4th	Normalized mutual information	2.3881
Cubic Lagrange	Correlation ratio	2.3649
Cubic Lagrange	Least squares	2.3613
Cubic Lagrange	Normalized cross correlation	2.3615
Cubic Lagrange	Normalized mutual information	2.3636
Quintic Lagrange	Correlation ratio	2.3527
Quintic Lagrange	Least squares	2.3559
Quintic Lagrange	Normalized cross correlation	2.3534
Quintic Lagrange	Normalized mutual information	2.3544
Heptic Lagrange	Correlation ratio	2.3549
Heptic Lagrange	Least squares	2.3561
Heptic Lagrange	Normalized cross correlation	2.3511
Heptic Lagrange	Normalized mutual information	2.3517
Windowed Sinc	Correlation ratio	2.3425
Windowed Sinc	Least squares	2.3452
Windowed Sinc	Normalized cross correlation	2.3434
Windowed Sinc	Normalized mutual information	2.3443

Table 8: The CR, MI, NMI, and NCC of reference and registered images. The 3D registered images using trilinear, B-spline 3rd, B-spline 4th, cubic Lagrange, quintic Lagrange, heptic Lagrang, windowed Sinc interpolations, and cost functions of CR, LS, NCC, and NM.

	Registration	Pixel similarity cost functions			
Interpolation	Cost function	Correlation Ration	Mutual Information	Normalized Mutual Information	Normalized Cross Correlation
Trilinear	Correlation Ratio	0.030921	0.572625	0.758732	0.016443
Trilinear	Least Square	0.030943	0.575558	0.758843	0.016472
Trilinear	Normalized Cross correlation	0.030978	0.577968	0.758742	0.016498
Trilinear	Normalized Mutual Information	0.030874	0.571644	0.758756	0.016452
B-spline 3rd	Correlation Ratio	0.091192	0.906945	0.789837	0.047106
B-spline 3rd	Least Square	0.091371	0.905995	0.790105	0.047204
B-spline 3rd	Normalized Cross correlation	0.089311	0.905822	0.788936	0.046135
B-spline 3rd	Normalized Mutual Information	0.091554	0.906234	0.78986	0.047101
B-spline 4th	Correlation Ratio	0.047523	0.645413	0.764792	0.026291
B-spline 4th	Least Square	0.047664	0.647675	0.764965	0.026334
B-spline 4th	Normalized Cross correlation	0.047837	0.646529	0.764938	0.026347
B-spline 4th	Normalized Mutual Information	0.047741	0.646291	0.764879	0.026328
Cubic Lagrange	Correlation Ratio	0.027451	0.557755	0.738121	0.014453
Cubic Lagrange	Least Square	0.027678	0.559016	0.738517	0.014556
Cubic Lagrange	Normalized Cross correlation	0.027751	0.557785	0.738253	0.014558
Cubic Lagrange	Normalized Mutual Information	0.027632	0.558993	0.734889	0.014486
Quintic Lagrange	Correlation Ratio	0.026226	0.533578	0.731717	0.013931
Quintic Lagrange	Least Square	0.026307	0.538433	0.730597	0.014006
Quintic Lagrange	Normalized Cross correlation	0.026227	0.533604	0.731881	0.013986
Quintic Lagrange	Normalized Mutual Information	0.026234	0.532218	0.731289	0.013912
Heptic Lagrange	Correlation Ratio	0.025983	0.537712	0.729622	0.013651
Heptic Lagrange	Least Square	0.026274	0.532524	0.731221	0.013767
Heptic Lagrange	Normalized Cross correlation	0.026273	0.531087	0.730581	0.013741
Heptic Lagrange	Normalized Mutual Information	0.026162	0.531199	0.730681	0.013672
Windowed Sinc	Correlation Ratio	0.024201	0.263132	0.720291	0.013392
Windowed Sinc	Least Square	0.025253	0.260997	0.720884	0.013445
Windowed Sinc	Normalized Cross correlation	0.024727	0.266973	0.720306	0.013544
Windowed Sinc	Normalized Mutual Information	0.024819	0.262372	0.730032	0.013426

4.3 Results of Super Resolution Technique

The 3D MSE and PSNR are tabulated in Table 9 for 256-sized MRI images in 3D. The 3-D data sets used for the validation of the original information preservation method were anatomical volumes in the axial (256*256*128), sagittal (256*120*256), and coronal (120*256*256) planes. Each was mapped to 256*256*256 grid preserving original data and combined. My method yielded more accurate results than interpolating each plane separately. As shown in Appendix A, combining the data from the three planes reduced the MSE significantly in comparison with the individual volumes.

Table 9:3D MSE and PSNR for MR images of 256 for Axial, sagittal, coronal, and combined three volumes.

	MSE	PSNR(dB)
Axial view	0.002743	111.43
Sagittal view	0.002821	110.98
Coronal view	0.002783	111.22
Combined	0.002191	116.48

The runtimes of each plane and combined the data were computed. The interpolation and registration of axial view (256*256*128) took approximately 184 s. The sagittal and coronal views required around 190 and 193 s for 3D MR images of 256*120*256 and 120*256*256, respectively. Compared with the axial view took 4.89% of the coronal view time. In general, the combined data took a bit more time than each plane separately. The combined data took about 1.5 times as long as axial, sagittal, and coronal views.

4.3.1 Visual Quality of Reconstructed Images

For MRI, combining the datasets would lead to mis-mapping of data. I removed this misalignment with the registration method. The axial, sagittal, and coronal planes are demonstrated in Figure 28 for the brain along with the new combined dataset. Visually inspecting each scan demonstrates higher quality images for each orientation, respectively, and lower quality for the other two. This was the case in all three planes; the quality was better than just in the axial, sagittal, and coronal planes. For instance, the top row (axial plane) demonstrated better quality for the first row (axial perspective) and worse quality for the other two.

I also computed the joint histograms of axial, sagittal, and coronal planes for the brain along the 3D combined datasets in order to evaluate the accuracy of SRR method (See Figure 28).

I have introduced my method to exploit the original information from MRI data using different planes to increase resolution and SNR. Thus, by scanning in two or three different planes, I am adding new information, specifically since the in-plane resolution (xy) is usually higher than the slice thickness (z). This is recommended since small *voxels* have lower SNR, so the high spatial resolution image may be too noisy to be diagnostically useful if the *voxels* are too small for adequate signal. Also, it is known that small *voxels* are particularly a problem on low-field imaging systems. This problem is alleviated by my technique since I combined information from the in-plane resolution of

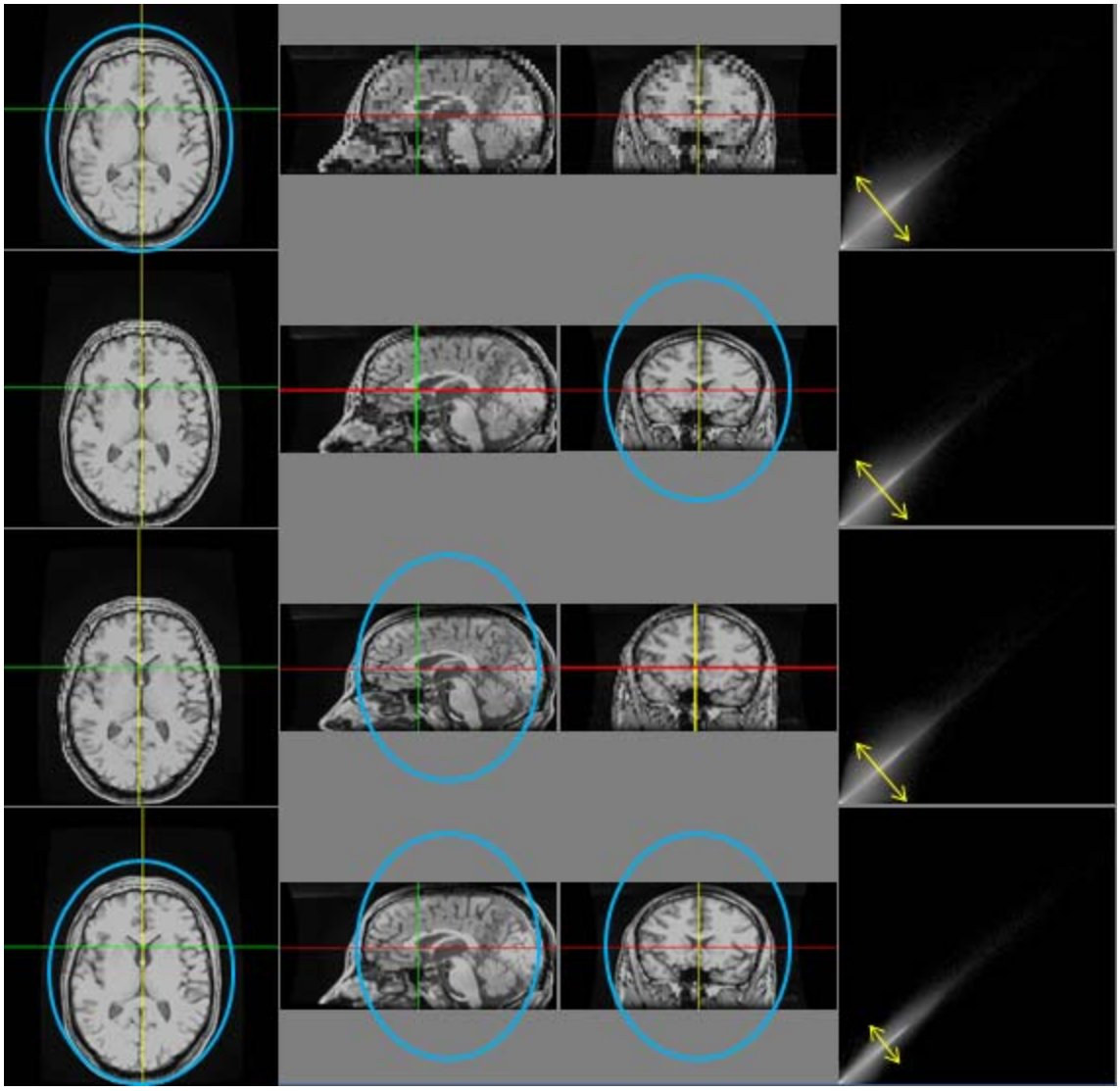

Figure 28: Brain images of the axial, coronal, sagittal, and combined datasets (top to bottom). Each column displays the axial, coronal and sagittal perspectives (left to right). Joint histogram for the combined datasets is similar (with reference datasets) and all gray value correspondences lie on the diagonal with minor dispersion: axial, coronal, and sagittal show the histograms with major dispersion.

another plane and thus we do not have to decrease the *voxel* size at the time of acquisition.

In many clinical protocols, the interslice distance plus the slice thickness can be up to eight times that of the in-plane resolution. In such cases, it may become difficult to reconstruct isotropic volumes using three LR scans. In this situation, possibilities of combining additional oblique scans and optimizing the interpolation technique would alleviate this issue [76].

5 Conclusion and Future Work

The interpolation techniques play a critical role in the improvement and deterioration of the quality of the image as the resolution changes. Thus, the interpolation error is very crucial to assess the interpolation techniques. The interpolation error depends on some features like geometric deformation and the content of the image; therefore only one evaluation method would not be adequate to evaluate all properties of an algorithm, and a variety of methods should be applied. The comparison is performed by visual quality assessment, quantitative interpolation error determination, and run time measurement based on clinical images. In this study, the results of the algorithms showed the trilinear method has the smallest interpolation error and highest PSNR and is one of the fastest techniques, making it appropriate for upsampling in super resolution. Although super powerful computers are able to compute a huge amount of data in real time, fast methods might be required for online re-sampling of image sequences or films [77]. The resulting images for trilinear interpolation are less smooth and blocky than other interpolated images. Nevertheless, trilinear interpolation has the effect of losing some high frequency information from the image [78]. Equivalent conclusions have been drawn about the relative advantage of trilinear in studies of the [79-81] of the registration and repeated sectioning of MR images.

Also, the effect of cost functions (LS, NMI, NCC and CR), and interpolations (trilinear, cubic Lagrange, quintic Lagrange, heptic Lagrange, windowed Sinc, B-spline 3rd, and B-Spline 4th) for OAIR of 3D brain images were examined, and my

experimental results showed interpolations can effectively decrease or increase the failure possibility of the registration algorithm, and the robustness of method was not due to the choice of cost function, but the choice of interpolation was critical on the robustness of registration. In addition, each component of the optimization method was also necessary to achieve the strong registrations.

I noted that the study presented in Tables and Figures relied on the same modality (MRI); in addition, these results are not representative of different modality combinations. Perhaps other conclusions would be obtained by the use of different modality combinations or transformations, for instance, MRI-PET or CT-MRI.

Also, OAIR was explained in detail, and it was a powerful image registration algorithm. This algorithm was a fully automated algorithm and proposed various re-sampling interpolation methods combined with CR, LS, NCC, and NMI as a cost function. One of the advantages of this method is using a feature detector (corners are used as the features) to automatically choose a large number of potentially matchable feature points in both images. The algorithm is able to detect identical features in all projections of the scene regardless of the particular image deformation. This method has direct potential for registering clinical MRI images. We have validated this method quantitatively and qualitatively, on the simulated and real data, respectively. Also, there are many excellent sources for more in-depth discussions of image registration [82-85].

The goal of this thesis was to introduce a method for utilizing the original information from more than one MRI volume in order to increase the resolution. This

method has direct potential for enhancing clinical MRI resolution. This new technique can be utilized for reducing artifact data loss by utilizing non-isotropic volumes of the same object and combining them to extract the most information from all the volumes. This ability to combine information will enrich the data sets by both enhancing the image for visualization and the data for further computational processing.

5.1 Future Work

There are several ways to expand on this thesis. One way is to use different modalities, i.e., CT-MRI or MRI-PET. Another way would be to change different transformations during registration, i.e., affine or rigid or global rescale. Finally, a more comprehensive study could be done by applying different cost functions and interpolations on different modalities.

Appendix A: Tables of Interpolation and Registration and SRR Results

A.1: Statistical analysis of 3D MSE for MR image of 256*256*60, 256*128*120, and 128*256*120 for interpolations of trilinear, nearest neighbor, B-spline 3rd, B-spline 4th, cubic Lagrangian, quintic Lagrangian, heptic Lagrangian, windowed Sin (comparison for all pairs using Tukey's honest significance test (HSD)).

Interpolation	Interpolation	Difference	Std Err Dif	Lower CL	Upper CL	p-Value
Nearest Neighbor	Trilinear	0.0130180	0.0005809	0.011007	0.0150291	<.0001
Nearest Neighbor	Heptic Lagrange	0.0109340	0.0005809	0.008923	0.0129451	<.0001
Nearest Neighbor	Quintic Lagrange	0.0108070	0.0005809	0.008796	0.0128181	<.0001
Nearest Neighbor	Cubic Lagrange	0.0107907	0.0005809	0.008780	0.0128018	<.0001
Nearest Neighbor	Windowed Sinc	0.0107000	0.0005809	0.008689	0.0127111	<.0001
Bspline 3rd	Trilinear	0.0093993	0.0005809	0.007388	0.0114105	<.0001
Nearest Neighbor	Bspline 4th	0.0089617	0.0005809	0.006951	0.0109728	<.0001
Bspline 3rd	Heptic Lagrange	0.0073153	0.0005809	0.005304	0.0093265	<.0001
Bspline 3rd	Quintic Lagrange	0.0071883	0.0005809	0.005177	0.0091995	<.0001
Bspline 3rd	Cubic Lagrange	0.0071720	0.0005809	0.005161	0.0091831	<.0001
Bspline 3rd	Windowed Sinc	0.0070813	0.0005809	0.005070	0.0090925	<.0001
Bspline 3rd	Bspline 4th	0.0053430	0.0005809	0.003332	0.0073541	<.0001
Bspline 4th	Trilinear	0.0040563	0.0005809	0.002045	0.0060675	<.0001
Nearest Neighbor	Bspline 3rd	0.0036187	0.0005809	0.001608	0.0056298	0.0003
Windowed Sinc	Trilinear	0.0023180	0.0005809	0.000307	0.0043291	0.0182
Cubic Lagrange	Trilinear	0.0022273	0.0005809	0.000216	0.0042385	0.0246
Quintic Lagrange	Trilinear	0.0022110	0.0005809	0.000200	0.0042221	0.0260
Heptic Lagrange	Trilinear	0.0020840	0.0005809	0.000073	0.0040951	0.0395
Bspline 4th	Heptic Lagrange	0.0019723	0.0005809	-0.000039	0.0039835	0.0566
Bspline 4th	Quintic Lagrange	0.0018453	0.0005809	-0.000166	0.0038565	0.0845
Bspline 4th	Cubic Lagrange	0.0018290	0.0005809	-0.000182	0.0038401	0.0889
Bspline 4th	Windowed Sinc	0.0017383	0.0005809	-0.000273	0.0037495	0.1172
Windowed Sinc	Heptic Lagrange	0.0002340	0.0005809	-0.001777	0.0022451	0.9999
Cubic Lagrange	Heptic Lagrange	0.0001433	0.0005809	-0.001868	0.0021545	1.0000

A. 2: Connecting letters for interpolated images (interpolations not connected by same letter are significantly different) (from Tukey's honest significance test (HSD)), HSD=0.05.

Interpolation	Letter Column A	Letter Column B	Letter Column C	Letter Column D	Mean
Nearest Neighbor	A				0.01588333
Bspline 3rd		B			0.01226467
Bspline 4th			C		0.00692167
Windowed Sinc			C		0.00518333
Cubic Lagrange			C		0.00509267
Quintic Lagrange			C		0.00507633
Heptic Lagrange			C		0.00494933
Trilinear				D	0.00286533

A. 3: Statistical analysis of MR image of matrix sizes of 256*256*60, 256*128*120, and 128*256*120 (comparison for all pairs using Tukey's honest significance test (HSD).

Matrix sizes	Matrix sizes	Difference	Std Err Diff	Lower CL	Upper CL	p-value
256*128*120	256*256*60	0.0011246	0.0022250	-0.004484	0.0067328	0.8695
128*256*120	256*256*60	0.0010056	0.0022250	-0.004603	0.0066138	0.9984
256*128*120	128*256*120	0.0001190	0.0022250	-0.005489	0.0057272	0.9984

A. 4: Statistical analysis of 3D MSE for MR image for registered image of 256*256*120 using cost functions of CR, LS, NCC, and NMI (comparison for all pairs using Tukey's honest significance test (HSD)).

Cost Function	Cost Function	Difference	Std Err Diff	Lower CL	Upper CL	p-value
Least squares	Normalized cross correlation	0.0001854	0.0091292	-0.024999	0.0253694	1.0000
Least squares	Correlation ratio	0.0001180	0.0091292	-0.025066	0.0253020	1.0000
Normalized mutual information	Normalized cross correlation	0.0001156	0.0091292	-0.025068	0.0252996	1.0000
Least squares	Normalized mutual information	0.0000699	0.0091292	-0.025114	0.0252539	1.0000
Correlation ratio	Normalized cross correlation	0.0000674	0.0091292	-0.025117	0.0252514	1.0000
Normalized mutual information	Correlation ratio	0.0000481	0.0091292	-0.025136	0.0252322	1.0000

A. 5: Connecting letters for registered images using different cost functions (cost functions not connected by same letter are significantly different) (from Tukey's honest significance test (HSD)).

Interpolation	Letter Column A	Mean
Least squares	A	0.02955357
Normalized mutual information	A	0.02948371
Correlation ratio	A	0.02943557
Normalized cross correlation	A	0.02936814

A. 6*:* Statistical analysis of 3D MSE for MR image for registered image of 256*256*120 using interpolations of trilinear, B-spline 3rd , B-spline 4th, cubic Lagrange, quintic Lagrange, heptic Lagrangian, windowed Sinc and cost functions of CR, LS, NCC, and NMI (comparison for all pairs using Tukey's honest significance test (HSD)).

Interpolation	Interpolation	Difference	Std Err Diff	Lower CL	Upper CL	p-value
Bspline 3rd	Windowed Sinc	0.0461063	0.0001842	0.045508	0.0467049	<.0001
Bspline 3rd	Heptic Lagrange	0.0456225	0.0001842	0.045024	0.0462212	<.0001
Bspline 3rd	Quintic Lagrange	0.0452680	0.0001842	0.044669	0.0458667	<.0001
Bspline 3rd	Cubic Lagrange	0.0444823	0.0001842	0.043884	0.0450809	<.0001
Bspline 3rd	Trilinear	0.0417268	0.0001842	0.041128	0.0423254	<.0001
Bspline 3rd	Bspline 4^{th}	0.0277128	0.0001842	0.027114	0.0283114	<.0001
Bspline 4th	Windowed Sinc	0.0183935	0.0001842	0.017795	0.0189922	<.0001
Bspline 4th	Heptic Lagrange	0.0179098	0.0001842	0.017311	0.0185084	<.0001
Bspline 4th	Quintic Lagrange	0.0175553	0.0001842	0.016957	0.0181539	<.0001
Bspline 4th	Cubic Lagrange	0.0167695	0.0001842	0.016171	0.0173682	<.0001
Bspline 4th	Trilinear	0.0140140	0.0001842	0.013415	0.0146127	<.0001
Trilinear	Windowed Sinc	0.0043795	0.0001842	0.003781	0.0049782	<.0001
Trilinear	Heptic Lagrange	0.0038958	0.0001842	0.003297	0.0044944	<.0001
Trilinear	Quintic Lagrange	0.0035413	0.0001842	0.002943	0.0041399	<.0001
Trilinear	Cubic Lagrange	0.0027555	0.0001842	0.002157	0.0033542	<.0001
Cubic Lagrange	Windowed Sinc	0.0016240	0.0001842	0.001025	0.0022227	<.0001
Cubic Lagrange	Heptic Lagrange	0.0011402	0.0001842	0.000542	0.0017389	<.0001
Quintic Lagrange	Windowed Sinc	0.0008383	0.0001842	0.000240	0.0014369	0.0028
Cubic Lagrange	Quintic Lagrange	0.0007858	0.0001842	0.000187	0.0013844	0.0054
Heptic Lagrange	Windowed Sinc	0.0004838	0.0001842	-0.000115	0.0010824	0.1677
Quintic Lagrange	Heptic Lagrange	0.0003545	0.0001842	-0.000244	0.0009532	0.4869

A. 7*:* Connecting letters for registered images using different interpolations (interpolations not connected by same letter are significantly different) (from Tukey's honest significance test (HSD)), HSD=0.05.

Interpolation	Letter Column A	Letter Column B	Letter Column C	Letter Column D	Letter Column E	Letter Column F	Mean
Bspline 3rd	A						0.06530575
Bspline 4th		B					0.03759300
Trilinear			C				0.02357900
Cubic Lagrange				D			0.02082350
Quintic Lagrange					E		0.02003775
Heptic Lagrange					E		0.01968325
Windowed Sinc						F	0.01919950

A. 8*:* Statistical analysis of the joint entropy for the registered image of 256*256*120 using cost functions of CR, LS, NCC, and NMI (comparison for all pairs using Tukey's honest significance test (HSD)).

Cost Function	Cost Function	Difference	Std Err Diff	Lower CL	Upper CL	p-value
Normalized mutual information	Normalized cross correlation	0.0022714	0.0193411	-0.051083	0.0556260	0.9994
Least squares	Normalized cross correlation	0.0014286	0.0193411	-0.051926	0.0547831	0.9999
Normalized mutual information	Correlation ratio	0.0013000	0.0193411	-0.052055	0.0546546	0.9999
Correlation ratio	Normalized cross correlation	0.0009714	0.0193411	-0.052383	0.0543260	1.0000
Normalized mutual information	Least squares	0.0008429	0.0193411	-0.052512	0.0541974	1.0000
Least squares	Correlation ratio	0.0004571	0.0193411	-0.052897	0.0538117	1.0000

A. 9: Connecting letters of the joint entropy for the registered images using different cost functions (cost functions not connected by same letter are significantly different) (from Tukey's honest significance test (HSD)).

Interpolation	Letter Column A	Mean
Least squares	A	0.02955357
Normalized mutual information	A	0.02948371
Correlation ratio	A	0.02943557
Normalized cross correlation	A	0.02936814

A. 10: Statistical analysis of the joint entropy for the registered image of 256*256*120 using interpolations of trilinear, B-spline 3rd, B-spline 4th, cubic Lagrange, quintic Lagrange, heptic Lagrange, windowed Sinc and cost functions of CR, LS, NCC, and NMI (comparison for all pairs using Tukey's honest significance test (HSD)).

Interpolation	Interpolation	Difference	Std Err Diff	Lower CL	Upper CL	p-value
Bspline 3rd	Windowed Sinc	0.1062250	0.0014699	0.101447	0.1110033	<.0001
Bspline 3rd	Heptic Lagrange	0.0966250	0.0014699	0.091847	0.1014033	<.0001
Bspline 3rd	Quintic Lagrange	0.0959750	0.0014699	0.091197	0.1007533	<.0001
Bspline 3rd	Cubic Lagrange	0.0872500	0.0014699	0.082472	0.0920283	<.0001
Bspline 3rd	Trilinear	0.0767750	0.0014699	0.071997	0.0815533	<.0001
Bspline 3rd	Bspline 4^{th}	0.0617000	0.0014699	0.056922	0.0664783	<.0001
Bspline 4th	Windowed Sinc	0.0445250	0.0014699	0.039747	0.0493033	<.0001
Bspline 4th	Heptic Lagrange	0.0349250	0.0014699	0.030147	0.0397033	<.0001
Bspline 4th	Quintic Lagrange	0.0342750	0.0014699	0.029497	0.0390533	<.0001
Trilinear	Windowed Sinc	0.0294500	0.0014699	0.024672	0.0342283	<.0001
Bspline 4th	Cubic Lagrange	0.0255500	0.0014699	0.020772	0.0303283	<.0001
Trilinear	Heptic Lagrange	0.0198500	0.0014699	0.015072	0.0246283	<.0001
Trilinear	Quintic Lagrange	0.0192000	0.0014699	0.014422	0.0239783	<.0001
Cubic Lagrange	Windowed Sinc	0.0189750	0.0014699	0.014197	0.0237533	<.0001
Bspline 4th	Trilinear	0.0150750	0.0014699	0.010297	0.0198533	<.0001
Trilinear	Cubic Lagrange	0.0104750	0.0014699	0.005697	0.0152533	<.0001
Quintic Lagrange	Windowed Sinc	0.0102500	0.0014699	0.005472	0.0150283	<.0001
Heptic Lagrange	Windowed Sinc	0.0096000	0.0014699	0.004822	0.0143783	<.0001
Cubic Lagrange	Heptic Lagrange	0.0093750	0.0014699	0.004597	0.0141533	<.0001
Cubic Lagrange	Quintic Lagrange	0.0087250	0.0014699	0.003947	0.0135033	0.0001
Quintic Lagrange	Heptic Lagrange	0.0006500	0.0014699	-0.004128	0.0054283	0.9993

A. 11: Connecting letters of the joint entropy for the registered images using different interpolations (interpolations not connected by same letter are significantly different) (from Tukey's honest significance test (HSD)), HSD=0.05.

Interpolation	Letter Column A	Letter Column B	Letter Column C	Letter Column D	Letter Column E	Letter Column F	Mean
Bspline 3rd	A						2.4500750
Bspline 4th		B					2.3883750
Trilinear			C				2.3733000
Cubic Lagrange				D			2.3628250
Quintic Lagrange					E		2.3541000
Heptic Lagrange					E		2.3534500
Windowed Sinc						F	2.3438500

A. 12*:* Statistical analysis of CR of reference and the registered images. The registered images using cost functions of CR, LS, NCC, and NMI (comparison for all pairs using Tukey's honest significance test (HSD)).

Cost Function	Cost Function	Difference	Std Err Diff	Lower CL	Upper CL	p-value
Least Square	Correlation Ratio	0.0003561	0.0128419	-0.035070	0.0357818	1.0000
Normalized Mutual Information	Correlation Ratio	0.0003413	0.0128419	-0.035084	0.0357669	1.0000
Least Square	Normalized Cross correlation	0.0002123	0.0128419	-0.035213	0.0356379	1.0000
Normalized Mutual Information	Normalized Cross correlation	0.0001974	0.0128419	-0.035228	0.0356231	1.0000
Normalized Cross correlation	Correlation Ratio	0.0001439	0.0128419	-0.035282	0.0355695	1.0000
Least Square	Normalized Mutual Information	0.0000149	0.0128419	-0.035411	0.0354405	1.0000

A. 13: Connecting letters of CR for the registered images using different cost functions (cost functions not connected by same letter are significantly different) (from Tukey's honest significance test (HSD)).

Interpolation	Letter Column A	Mean
Least Square	A	0.03947000
Normalized Mutual Information	A	0.03945514
Normalized Cross correlation	A	0.03925771
Correlation Ratio	A	0.03911381

A. 14: Statistical analysis of CR of reference and registered images. The 3D registered images using Trilinear, B-spline 3rd, B-spline 4th, Cubic Lagrange, quintic Lagrange, heptic Lagrang, windowed Sinc interpolations and cost functions of CR, LS, NCC, and NMI.

Interpolation	Interpolation	Difference	Std Err Diff	Lower CL	Upper CL	p-value
B-spline 3rd	Windowed Sinc	0.0661070	0.0003079	0.065106	0.0671078	<.0001
B-spline 3rd	Heptic Lagrange	0.0646840	0.0003079	0.063683	0.0656848	<.0001
B-spline 3rd	Quintic Lagrange	0.0646085	0.0003079	0.063608	0.0656093	<.0001
B-spline 3rd	Cubic Lagrange	0.0632290	0.0003079	0.062228	0.0642298	<.0001
B-spline 3rd	Trilinear	0.0599280	0.0003079	0.058927	0.0609288	<.0001
B-spline 3rd	B-spline 4^{th}	0.0431658	0.0003079	0.042165	0.0441665	<.0001
B-spline 4th	Windowed Sinc	0.0229413	0.0003079	0.021940	0.0239420	<.0001
B-spline 4th	Heptic Lagrange	0.0215183	0.0003079	0.020517	0.0225190	<.0001
B-spline 4th	Quintic Lagrange	0.0214428	0.0003079	0.020442	0.0224435	<.0001
B-spline 4th	Cubic Lagrange	0.0200633	0.0003079	0.019062	0.0210640	<.0001
B-spline 4th	Trilinear	0.0167623	0.0003079	0.015761	0.0177630	<.0001
Trilinear	Windowed Sinc	0.0061790	0.0003079	0.005178	0.0071798	<.0001
Trilinear	Heptic Lagrange	0.0047560	0.0003079	0.003755	0.0057568	<.0001
Trilinear	Quintic Lagrange	0.0046805	0.0003079	0.003680	0.0056813	<.0001
Trilinear	Cubic Lagrange	0.0033010	0.0003079	0.002300	0.0043018	<.0001
Cubic Lagrange	Windowed Sinc	0.0028780	0.0003079	0.001877	0.0038788	<.0001
Quintic Lagrange	Windowed Sinc	0.0014985	0.0003079	0.000498	0.0024993	0.0014
Cubic Lagrange	Heptic Lagrange	0.0014550	0.0003079	0.000454	0.0024558	0.0019
Heptic Lagrange	Windowed Sinc	0.0014230	0.0003079	0.000422	0.0024238	0.0024
Cubic Lagrange	Quintic Lagrange	0.0013795	0.0003079	0.000379	0.0023803	0.0033
Quintic Lagrange	Heptic Lagrange	0.0000755	0.0003079	-0.000925	0.0010763	1.0000

A. 15: Connecting letters of CR for the registered images using different interpolations (interpolations not connected by same letter are significantly different) (from Tukey's honest significance test (HSD)), HSD=0.05.

Interpolation	Letter Column A	Letter Column B	Letter Column C	Letter Column D	Letter Column E	Letter Column F	Mean
B-spline 3rd	A						0.09085700
B-spline 4th		B					0.04769125
Trilinear			C				0.03092900
Cubic Lagrange				D			0.02762800
Quintic Lagrange					E		0.02624850
Heptic Lagrange					E		0.02617300
Windowed Sinc						F	0.02475000

A. 16: Statistical analysis of MI of reference and the registered images. The registered images using cost functions of CR, LS, NCC, and NMI (comparison for all pairs using Tukey's honest significance test (HSD)).

Cost Function	Cost Function	Difference	Std Err Diff	Lower CL	Upper CL	p-value
Least Square	Normalized Mutual Information	0.0016067	0.1013326	-0.277930	0.2811437	1.0000
Normalized Cross correlation	Normalized Mutual Information	0.0015453	0.1013326	-0.277992	0.2810823	1.0000
Correlation Ratio	Normalized Mutual Information	0.0011727	0.1013326	-0.278364	0.2807097	1.0000
Least Square	Correlation Ratio	0.0004340	0.1013326	-0.279103	0.2799710	1.0000
Normalized Cross correlation	Correlation Ratio	0.0003726	0.1013326	-0.279164	0.2799096	1.0000
Least Square	Normalized Cross correlation	0.0000614	0.1013326	-0.279476	0.2795985	1.0000

A. 17: Connecting letters of MI for the registered images using different cost functions (cost functions not connected by same letter are significantly different) (from Tukey's honest significance test (HSD)).

Interpolation	Letter Column A	Mean
Least Square	A	0.57431400
Normalized Cross correlation	A	0.57425257
Correlation Ratio	A	0.57388000
Normalized Mutual Information	A	0.57270729

A. 18: Statistical analysis of MI of reference and registered images. The 3D registered images using Trilinear, B-spline 3rd, B-spline 4th, Cubic Lagrange, quintic Lagrange, heptic Lagrang, windowed Sinc interpolations and cost functions of CR, LS, NCC, and NMI.

Interpolation	Interpolation	Difference	Std Err Diff	Lower CL	Upper CL	p-value
B-spline 3rd	Windowed Sinc	0.6428805	0.0015501	0.637841	0.6479196	<.0001
B-spline 4th	Windowed Sinc	0.3831085	0.0015501	0.378069	0.3881476	<.0001
B-spline 3rd	Heptic Lagrange	0.3731185	0.0015501	0.368079	0.3781576	<.0001
B-spline 3rd	Quintic Lagrange	0.3717908	0.0015501	0.366752	0.3768299	<.0001
B-spline 3rd	Cubic Lagrange	0.3478618	0.0015501	0.342823	0.3529009	<.0001
B-spline 3rd	Trilinear	0.3318003	0.0015501	0.326761	0.3368394	<.0001
Trilinear	Windowed Sinc	0.3110803	0.0015501	0.306041	0.3161194	<.0001
Cubic Lagrange	Windowed Sinc	0.2950188	0.0015501	0.289980	0.3000579	<.0001
Quintic Lagrange	Windowed Sinc	0.2710898	0.0015501	0.266051	0.2761289	<.0001
Heptic Lagrange	Windowed Sinc	0.2697620	0.0015501	0.264723	0.2748011	<.0001
B-spline 3rd	B-spline 4^{th}	0.2597720	0.0015501	0.254733	0.2648111	<.0001
B-spline 4th	Heptic Lagrange	0.1133465	0.0015501	0.108307	0.1183856	<.0001
B-spline 4th	Quintic Lagrange	0.1120187	0.0015501	0.106980	0.1170579	<.0001
B-spline 4th	Cubic Lagrange	0.0880897	0.0015501	0.083051	0.0931289	<.0001
B-spline 4th	Trilinear	0.0720283	0.0015501	0.066989	0.0770674	<.0001
Trilinear	Heptic Lagrange	0.0413183	0.0015501	0.036279	0.0463574	<.0001
Trilinear	Quintic Lagrange	0.0399905	0.0015501	0.034951	0.0450296	<.0001
Cubic Lagrange	Heptic Lagrange	0.0252568	0.0015501	0.020218	0.0302959	<.0001
Cubic Lagrange	Quintic Lagrange	0.0239290	0.0015501	0.018890	0.0289681	<.0001
Trilinear	Cubic Lagrange	0.0160615	0.0015501	0.011022	0.0211006	<.0001
Quintic Lagrange	Heptic Lagrange	0.0013278	0.0015501	-0.003711	0.0063669	0.9753

A. 19*:* Connecting letters of MI for the registered images using different interpolations (interpolations not connected by same letter are significantly different) (from Tukey's honest significance test (HSD)), HSD=0.05.

Interpolation	Letter Column A	Letter Column B	Letter Column C	Letter Column D	Letter Column E	Letter Column F	Mean
B-spline 3rd	A						0.90624900
B-spline 4th		B					0.64647700
Trilinear			C				0.57444875
Cubic Lagrange				D			0.55838725
Quintic Lagrange					E		0.53445825
Heptic Lagrange					E		0.53313050
Windowed Sinc						F	0.26336850

A. 20: Statistical analysis of NMI of reference and the registered images. The registered images using cost functions of CR, LS, NCC, and NMI (comparison for all pairs using Tukey's honest significance test (HSD)).

Cost Function	Cost Function	Difference	Std Err Diff	Lower CL	Upper CL	p-value
Normalized Mutual Information	Correlation Ratio	0.0010391	0.0128771	-0.034484	0.0365619	0.9998
Normalized Mutual Information	Normalized Cross correlation	0.0009641	0.0128771	-0.034559	0.0364869	0.9998
Normalized Mutual Information	Least Square	0.0007506	0.0128771	-0.034772	0.0362734	0.9999
Least Square	Correlation Ratio	0.0002886	0.0128771	-0.035234	0.0358114	1.0000
Least Square	Normalized Cross correlation	0.0002136	0.0128771	-0.035309	0.0357364	1.0000
Normalized Cross correlation	Correlation Ratio	0.0000750	0.0128771	-0.035448	0.0355978	1.0000

A. 21: Connecting letters of NMI for the registered images using different cost functions (cost functions not connected by same letter are significantly different) (from Tukey's honest significance test (HSD)).

Interpolation	Letter Column A	Mean
Normalized Mutual Information	A	0.74862657
Least Square	A	0.74787600
Normalized Cross correlation	A	0.74766243
Correlation Ratio	A	0.74758743

A. 22: Statistical analysis of NMI of reference and registered images. The 3D registered images using Trilinear, B-spline 3rd, B-spline 4th, Cubic Lagrange, Quintic Lagrange, Heptic Lagrang, Windowed Sinc interpolations and cost functions of CR, LS, NCC, and NMI.

Interpolation	Interpolation	Difference	Std Err Diff	Lower CL	Upper CL	p-value
B-spline 3rd	Windowed Sinc	0.0668063	0.0013834	0.062309	0.0713035	<.0001
B-spline 3rd	Heptic Lagrange	0.0591582	0.0013834	0.054661	0.0636555	<.0001
B-spline 3rd	Quintic Lagrange	0.0583135	0.0013834	0.053816	0.0628108	<.0001
B-spline 3rd	Cubic Lagrange	0.0522395	0.0013834	0.047742	0.0567368	<.0001
B-spline 4th	Windowed Sinc	0.0420153	0.0013834	0.037518	0.0465125	<.0001
Trilinear	Windowed Sinc	0.0358900	0.0013834	0.031393	0.0403873	<.0001
B-spline 4th	Heptic Lagrange	0.0343672	0.0013834	0.029870	0.0388645	<.0001
B-spline 4th	Quintic Lagrange	0.0335225	0.0013834	0.029025	0.0380198	<.0001
B-spline 3rd	Trilinear	0.0309163	0.0013834	0.026419	0.0354135	<.0001
Trilinear	Heptic Lagrange	0.0282420	0.0013834	0.023745	0.0327393	<.0001
B-spline 4th	Cubic Lagrange	0.0274485	0.0013834	0.022951	0.0319458	<.0001
Trilinear	Quintic Lagrange	0.0273972	0.0013834	0.022900	0.0318945	<.0001
B-spline 3rd	B-spline 4th	0.0247910	0.0013834	0.020294	0.0292883	<.0001
Trilinear	Cubic Lagrange	0.0213233	0.0013834	0.016826	0.0258205	<.0001
Cubic Lagrange	Windowed Sinc	0.0145667	0.0013834	0.010069	0.0190640	<.0001
Quintic Lagrange	Windowed Sinc	0.0084928	0.0013834	0.003995	0.0129900	<.0001
Heptic Lagrange	Windowed Sinc	0.0076480	0.0013834	0.003151	0.0121453	0.0003
Cubic Lagrange	Heptic Lagrange	0.0069187	0.0013834	0.002421	0.0114160	0.0010
B-spline 4th	Trilinear	0.0061253	0.0013834	0.001628	0.0106225	0.0037
Cubic Lagrange	Quintic Lagrange	0.0060740	0.0013834	0.001577	0.0105713	0.0041
Quintic Lagrange	Heptic Lagrange	0.0008447	0.0013834	-0.003653	0.0053420	0.9957

A. 23*:* Connecting letters of NMI for the registered images using different interpolations (interpolations not connected by same letter are significantly different) (from Tukey's honest significance test (HSD)), HSD=0.05.

Interpolation	Letter Column A	Letter Column B	Letter Column C	Letter Column D	Letter Column E	Letter Column F	Mean
B-spline 3rd	A						0.78968450
B-spline 4th		B					0.76489350
Trilinear			C				0.75876825
Cubic Lagrange				D			0.73744500
Quintic Lagrange					E		0.73137100
Heptic Lagrange					E		0.73052625
Windowed Sinc						F	0.72287825

A. 24: Statistical analysis of NCC of reference and the registered images. The registered images using cost functions of CR, LS, NCC, and NMI (comparison for all pairs using Tukey's honest significance test (HSD)).

Cost Function	Cost Function	Difference	Std Err Diff	Lower CL	Upper CL	p-value
Least Square	Normalized Cross correlation	0.0001393	0.0066210	-0.018126	0.0184042	1.0000
Normalized Mutual Information	Normalized Cross correlation	0.0000807	0.0066210	-0.018184	0.0183456	1.0000
Least Square	Correlation Ratio	0.0000740	0.0066210	-0.018191	0.0183389	1.0000
Correlation Ratio	Normalized Cross correlation	0.0000653	0.0066210	-0.018200	0.0183302	1.0000
Least Square	Normalized Mutual Information	0.0000586	0.0066210	-0.018206	0.0183235	1.0000
Normalized Mutual Information	Correlation Ratio	0.0000154	0.0066210	-0.018249	0.0182803	1.0000

A. 25: Connecting letters of NCC for the registered images using different cost functions (cost functions not connected by same letter are significantly different) (from Tukey's honest significance test (HSD)).

Interpolation	Letter Column A	Mean
Least Square	A	0.02082629
Normalized Mutual Information	A	0.02076771
Correlation Ratio	A	0.02075229
Normalized Cross correlation	A	0.02068700

A. 26: Statistical analysis of NCC of reference and registered images. The 3D registered images using Trilinear, B-spline 3rd, B-spline 4th, Cubic Lagrange, Quintic Lagrange, Heptic Lagrang, Windowed Sinc interpolations and cost functions of CR, LS, NCC, and NMI.

Interpolation	Interpolation	Difference	Std Err Diff	Lower CL	Upper CL	p-value
B-spline 3rd	Windowed Sinc	0.0334345	0.0001379	0.032986	0.0338829	<.0001
B-spline 3rd	Heptic Lagrange	0.0331793	0.0001379	0.032731	0.0336277	<.0001
B-spline 3rd	Quintic Lagrange	0.0329275	0.0001379	0.032479	0.0333759	<.0001
B-spline 3rd	Cubic Lagrange	0.0323730	0.0001379	0.031925	0.0328214	<.0001
B-spline 3rd	Trilinear	0.0304200	0.0001379	0.029972	0.0308684	<.0001
B-spline 3rd	B-spline 4^{th}	0.0205613	0.0001379	0.020113	0.0210097	<.0001
B-spline 4th	Windowed Sinc	0.0128733	0.0001379	0.012425	0.0133217	<.0001
B-spline 4th	Heptic Lagrange	0.0126180	0.0001379	0.012170	0.0130664	<.0001
B-spline 4th	Quintic Lagrange	0.0123663	0.0001379	0.011918	0.0128147	<.0001
B-spline 4th	Cubic Lagrange	0.0118118	0.0001379	0.011363	0.0122602	<.0001
B-spline 4th	Trilinear	0.0098588	0.0001379	0.009410	0.0103072	<.0001
Trilinear	Windowed Sinc	0.0030145	0.0001379	0.002566	0.0034629	<.0001
Trilinear	Heptic Lagrange	0.0027593	0.0001379	0.002311	0.0032077	<.0001
Trilinear	Quintic Lagrange	0.0025075	0.0001379	0.002059	0.0029559	<.0001
Trilinear	Cubic Lagrange	0.0019530	0.0001379	0.001505	0.0024014	<.0001
Cubic Lagrange	Windowed Sinc	0.0010615	0.0001379	0.000613	0.0015099	<.0001
Cubic Lagrange	Heptic Lagrange	0.0008062	0.0001379	0.000358	0.0012547	0.0001
Cubic Lagrange	Quintic Lagrange	0.0005545	0.0001379	0.000106	0.0010029	0.0094
Quintic Lagrange	Windowed Sinc	0.0005070	0.0001379	0.000059	0.0009554	0.0202
Heptic Lagrange	Windowed Sinc	0.0002553	0.0001379	-0.000193	0.0007037	0.5315
Quintic Lagrange	Heptic Lagrange	0.0002518	0.0001379	-0.000197	0.0007002	0.5469

A. 27: Connecting letters of NCC for the registered images using different interpolations (interpolations not connected by same letter are significantly different) (from Tukey's honest significance test (HSD)), HSD=0.05.

Interpolation	Letter Column A	Letter Column B	Letter Column C	Letter Column D	Letter Column E	Letter Column F	Mean
B-spline 3rd	A						0.04688625
B-spline 4th		B					0.02632500
Trilinear			C				0.01646625
Cubic Lagrange				D			0.01451325
Quintic Lagrange					E		0.01395875
Heptic Lagrange					E		0.01370700
Windowed Sinc						F	0.01345175

A. 28: Statistical analysis of 3D MSE for MR images of 256 for Axial, sagittal, coronal and combined three volumes.

Interpolation	Interpolation	Difference	Std Err Diff	Lower CL	Upper CL	p-value
Sagittal	Combined	0.0006300	9.1287093e-8	0.0006297	0.0006303	<.0001
Coronal	Combined	0.0005920	9.1287093e-8	0.0005917	0.0005923	<.0001
Axial	Combined	0.0005520	9.1287093e-8	0.0005517	0.0005523	<.0001
Sagittal	Axial	0.0000780	9.1287093e-8	0.0000777	0.0000783	<.0001
Coronal	Axial	0.0000400	9.1287093e-8	0.0000397	0.0000403	<.0001
Sagittal	Coronal	0.0000380	9.1287093e-8	0.0000377	0.0000383	<.0001
Sagittal	Combined	0.0006300	9.1287093e-8	0.0006297	0.0006303	<.0001

A. 29: Connecting letters of 3D MSE for MR images of 256 for Axial, sagittal, coronal and combined three volumes. (interpolations not connected by same letter are significantly different) (from Tukey's honest significance test (HSD)), HSD=0.05.

Interpolation	Letter Column A	Letter Column B	Letter Column C	Letter Column D	Mean
Sagittal	A				0.00282125
Coronal		B			0.00278325
Axial			C		0.00274325
Combined				D	0.00219125

A. 30: Statistical analysis of 3D PSNR for MR images of 256 for Axial, sagittal, coronal and combined three volumes.

Interpolation	Interpolation	Difference	Std Err Diff	Lower CL	Upper CL	p-value
Combined	Sagittal	5.500000	2.4333494e-8	5.500000	5.500000	<.0001
Combined	Coronal	5.260000	2.4333494e-8	5.260000	5.260000	<.0001
Combined	Axial	5.050000	2.4333494e-8	5.050000	5.050000	<.0001
Axial	Sagittal	0.450000	2.4333494e-8	0.450000	0.450000	<.0001
Coronal	Sagittal	0.240000	2.4333494e-8	0.240000	0.240000	<.0001
Axial	Coronal	0.210000	2.4333494e-8	0.210000	0.210000	<.0001
Combined	Sagittal	5.500000	2.4333494e-8	5.500000	5.500000	<.0001

A. 31: Connecting letters of 3D PSNR for MR images of 256 for Axial, sagittal, coronal and combined three volumes. (interpolations not connected by same letter are significantly different) (from Tukey's honest significance test (HSD)).

Interpolation	Letter Column A	Letter Column B	Letter Column C	Letter Column D	Mean
Combined	A				116.48000
Axial		B			111.43000
Coronal			C		111.22000
Sagittal				D	110.98000

Bibliography

[1] S. Ch. Park, M. .K. Park, M. G. Kang;"Super-resolution image reconstruction: a technical overview," Signal Processing Magazine, IEEE, vol.20, no.3, pp. 21- 36, May 2003.

[2] T. Komatsu, K. Aizawa, T. Igarashi, and T. Saito, "Signal-processing based method for acquiring very high resolution image with multiple cameras and its theoretical analysis," Proc. Inst. Elec. Eng., vol. 140, no. 1, pt. I, pp. 19-25, February 1993.

[3] N. H. Kashou, Development of Functional Studies and Methods to Better Understand Visual Function, PhD thesis, The Ohio State University, 2008.

[4] M. Irani, and S. Peleg. Improving resolution by image registration. Computer Vision, Graphics, and Image Processing, Graphical Models and Image Processing 53, pp. 231–239. May 1991.

[5] M. Irani, and S. Peleg. Motion analysis for image enhancement: Resolution,occlusion, and transparency. In Journal of Visual Communication and Image Representation, vol. 4, pp. 324–335, December 1993.

[6] J. G. Tamez-Pena, S. Totterman, and K. J. Parker, "MRI isotropic resolution reconstruction from two orthogonal scans," in Proceedings of SPIE, vol. 4322, pp. 87 – 97, 2001.

[7] H. Greenspan, G. Oz, N. Kiryati, and S. Peled, "MRI interslice reconstruction using super-resolution," Magnetic Resonance Imaging, vol. 20, pp. 437–446, 2002.

[8] S. Borman and R. L. Stevenson, "Super-resolution from image sequences a review," tech. rep., University of Notre Dame, 1998.

[9] R. C. Hardie, K. J. Barnard, J. G. Bognar, and E. E. Armstrong, "Joint MAP registration and high-resolution image estimation using a sequence of undersampled images," IEEE Transactions on Image Processing, vol. 6, no. 12, pp. 1621– 1633, 1997.

[10] R. C. Hardie, K. J. Barnard, J. G. Bognar, and E. A. Watson, "High-resolution image reconstruction from a sequence of rotated and translated frames and its application to an infrared imaging system," Optical Engineering, vol. 37, no. 1, pp. 247–260, 1998.

[11] Y. Bai, X. Han, and J. L. Prince, "Super-resolution Reconstruction of MR Brain Images," in Proc. of 38th Annual Conference on Information Sciences and Systems, Princeton, March 2004.

[12] S. Geman and D. Geman, "Stochastic relaxation, Gibbs distributions and the Bayesian restoration of images," IEEE Trans. Pattern Anal. Machine Intell, vol. 6, pp. 721–741, 1984.

[13] http://www.epilepsy.org.au/about-epilepsy/understanding-epilepsy/human-brain-seizures

[14] http://www.magnet.fsu.edu/education/tutorials/magnetacademy/mri/fullarticle.html.

[15] http://healthishblog.com/all-you-need-to-know-about-mris.

[16] http://www.valleyradiologyimaging.com/MRI.html &
http://www.mrprotocols.com/learnmri/book/Exercise4.pdf

[17] V. D. Weishaupt and B. Marincek, How Does MRI Work, An Introduction to the Physics and Function of Magnetic Resonance Imaging, Springer, 2006.

[18] H. Greenspan, G. Oz, N. Kiryati, S. Peled "MRI inter-slice reconstruction using super-resolution", Magnetic Resonance Imaging, vol. 20, pp.437-446, 2002.

[19] M. Sajjad, N. Khattak, and N. Jafri, " Image Magnification Using Adaptive Interpolation by Pixel Level Data-Dependent Geometrical Shapes, International Journal of Computer Science and Engineering, vol. 1, no 2.

[20] J. A. Parker, R. V. Kenyon, and D. E. Troxel, "Comparison of interpolating methods for image resampling," Medical Imaging, IEEE Transactions on, vol. MI-2, pp. 31–39, 1983.

[21] H. Hsieh and H. Andrews, "Cubic splines for image interpolation and digital filtering," Acoustics, Speech and Signal Processing, IEEE Transactions on, vol. 26, pp. 508-517, 1978.

[22] E. Maeland, "On the comparison of interpolation methods, "Medical Imaging, IEEE Transactions on, vol. 7, pp. 213-217, 1988.

[23] T. M. Lehmann, C. Gonner, and K. Spitzer, "Survey: interpolation methods in medical image processing," Medical Imaging, IEEE Transactions on, vol. 18, pp. 1049-1075, 1999.

[24] R. Keys, "Cubic convolution interpolation for digital image processing," Acoustics, Speech and Signal Processing, IEEE Transactions on, vol. 29, pp. 1153-1160, 1981.

[25] J. A. Parker, R. V. Kenyon, and D. E. Troxel, "Comparison of Interpolating Methods for Image Resampling," Medical Imaging, IEEE Transactions on, vol. 2, pp. 31-39, 1983.

[26] E. eri and N. nie, "Interpolation approaches and spline based resampling for MR images," in Health Informatics and Bioinformatics (HIBIT), 2010 5th International Symposium on, pp. 137-143, 2010.

[27] D. L. G. Hill and P. Batchelor, Medical Image Registration, Chapter 3, “Registration Methodology: Concepts and Algorithms”, Editor, Joseph V. Hajnal, Derek L.G.Hill, and David J. Hawkes, CRC Press, pp. 40-70, 2001.

[28] R. P. Woods, Handbook of Medical Image Processing and Analysis, Chapter 33, “Within-Modality Registration Using Intensity-Based Cost Functions”, Editor, N. Isaac, Academic Press, pp. 529-553, 2000.

[29] F. B. Hildebrand, Introduction to Numerical Analysis, New York: Dover, Second edition, 1974.

[30] F. Jean-Jacques and B. Delyon, "Min-max interpolators and Lagrange interpolation formula," in Circuits and Systems, 2002. ISCAS 2002. IEEE International Symposium on, pp. IV-429-IV-432 vol.4, 2002.

[31] C. Yaotsu and L. Chong-Dao, "Algebraic Decoding of a Class of Binary Cyclic Codes Via Lagrange Interpolation Formula," Information Theory, IEEE Transactions on, vol. 56, pp. 130-139, 2010.

[32] Paul Bourke, "Interpolation Methods", December 1999, http://paulbourke.net/miscellaneous/interpolation.

[33]http://mipav.cit.nih.gov/documentation/HTML%20Algorithms/InterplationMethods.html.

[34] http://www.cl.cam.ac.uk/teaching/1999/AGraphHCI/SMAG/node4.html.

[35] H. Du and W. Mei, "Image Resizing Using Exponential B-Spline Functions," in Image and Signal Processing, 2009. CISP '09. 2nd International Congress on, pp.1-5, 2009.

[36] M. Sung, H. J. Kim, E. K Kim, J. Y. Kwak, J. K. Yoo, and H. S. Yoo," Clinical Evaluation of JPEG2000 Compression for Digital Mammography", IEEE Transaction on Nuclear Science, vol. 49, no. 3, June 2002.

[37] K. Keung, L. L.Yu, Sh. Wang, "Mean-Variance-Skewness-Kurtosis-based Portfolio Optimization", vol. 2, pp. 292 - 297, 2006.

[38] D. N. Joanest and C. A. Gill, Comparing measures of sample skewness and kurtosis", The Statistician 47, Part 1, pp. 183-189, 1998.

[39] R. P. Woods, Handbook of Medical Image Processing and Analysis, Chapter 33 "Within-Modality Registration Using Intensity-Based Cost Functions", Editor, Isaac N. Bankman, Academic Press, pp. 529-536, 2000.

[40] P. E. Radau, P. J. Slomka, P. Julin, L. Svensson, and L.-O. Wahlund, “Evaluation of linear registration algorithms for brain SPECT and the errors due to hypoperfusion lesions,” Medical Physics., vol. 28, no. 8, pp. 1660–1668, 2001.

[41] J. M. Blackall, D. Rueckert, C. R. Maurer Jr., G. P. Penney, D. L. G. Hill, and D. J. Hawkes, “An image registration approach to automated calibration for freehand 3D ultrasound,” in Medical Image Computing and Computer-Assisted Intervention, Berlin, Germany: Springer-Verlag, vol. 1935, pp. 462–471. 2000.

[42] Y. E. Erdi, K. Rosenzweig, A. K. Erdi, H. A. Macapinlac, Y.-C. Hu, L. E. Braban, J. L. Humm, O. D. Squire, C.-S. Chui, S. M. Larson, and E. D. Yorke, “Radiotherapy treatment planning for patients with non-small cell lung cancer using positron emission tomography (PET),” Radiotherapy Oncol., vol. 62, no. 1, pp. 51–60, 2002.

[43] K. Van Laere, M. Koole, Y. D’Asseler, J. Versijpt, K. Audenaert, F. Dumont, and R. Dierckx, “Automated stereotactic standardization of brain SPECT receptor data using single-photon transmission images,” Nuclear. Medical, vol. 42, no. 2, pp. 361–375, 2001.

[44] J.-F. Mangin, C. Poupon, C. Clark, D. Le Bihan, and I. Bloch, “Eddycurrent distortion correction and robust tensor estimation for MR diffusion imaging,” in Medical Image Computing and Computer-Assisted Intervention, W. J. Niessen and M. A. Viergever, Eds. Berlin, Germany: Springer-Verlag, Lecture Notes in Computer Science, vol. 2208, pp. 186–194, 2001.

[45] P. Viola and W. M. Wells III, “Alignment by maximization of mutual information,” International Journal Computer Vision, vol. 24, no. 2, pp. 137–154, 1997.

[46] M. Jenkinson and S. Smith, “A global optimization method for robust affine registration of brain images,” Medical Image Analysis, vol. 5, no. 2, pp. 143–156, 2001.

[47] J. F. Mangin, C. Poupon, C. Clark, D. Le Bihan, and I. Bloch, “Eddycurrent distortion correction and robust tensor estimation for MR diffusion imaging,” in Medical Image Computing and Computer-Assisted Intervention, W. J. Niessen and M. A. Viergever, Eds. Berlin, Germany: Springer-Verlag, Lecture Notes in Computer Science.vol. 2208, pp. 186–194, 2001.

[48] J. V. Hajnal, D. L. G. Hill, and D. J. Hawkes, Eds., Medical Image Registration. Boca Raton, FL: CRC, 2001.

[49] D. L. G. Hill, P. G. Batchelor, M. Holden, and D. J. Hawkes, “Medical image registration,” Physics in Medicine and Biology, vol. 46, no. 3, pp. R1–R45, 2001.

[50] R.P.Woods, Handbook of Medical Image Processing and Analysis, Chapter 33 "Within-Modality Registration Using Intensity-Based Cost Functions", Editor, N. Isaac, Bankman, Academic Press, pp. 529-553, 2000.

[51] A. Roche, X. Pennec, M. Rudolph, D. P. Auer, G. Malandain, S. Ourselin, L. .VI. Auer, and Ayache,” Generalized Correlation Ratio for Rigid Registration of 3D Ultrasound with MR Images”, Institut National De Recherche En Informatique Et En Automatique, July 2000.

[52] A. Roche, G. Malandain, N. Ayache,” The Correlation Ratio as a New Similarity Measure for Multimodal Image Registartion”, springer, vol 1496 of LNCS, pp.1115-1124, 1998.

[53] P. J. Kostelec and S. Periaswamy, “Image Registration for MRI”, Modern Signal Processing, MSRI Publications , vol 46, 2003.

[54] C. Studholme, D.L.G. Hill, D.J. Hawkes, “An overlap invariant entropy measure of 3D medical image alignment”, Pattern Recognition, vol 32, pp.71–86, 1999.

[55] J. P. W. Pluim, J. B. A. Maintz, and M. A. Viergever,” Mutual information based registration of medical images: a survey”, vol. 22, no. 8, August 2003.

[56] E. R. E. Denton, M. Holden, E. Christ, J. M. Jarosz, D. Russell-Jones, J. Goodey, T. C. S. Cox, and D. L. G. Hill, "The identification of cerebral volume changes in treated growth hormone-deficient adults using serial 3D MR image processing," Journal Of Computer Assisted Tomography, vol. 24, no. 1, pp. 139–145, 2000.

[57] Y. E. Erdi, K. Rosenzweig, A. K. Erdi, H. A. Macapinlac, Y.-C. Hu, L. E. Braban, J. L. Humm, O. D. Squire, C.-S. Chui, S. M. Larson, and E. D. Yorke, "Radiotherapy treatment planning for patients with non-small cell lung cancer using positron emission tomography (PET)," Radiotherapy Oncology Journal, vol. 62, no. 1, pp. 51–60, 2002.

[58] M. Jenkinson, S. Smith," A global optimisation method for robust affine registration of brain images", Medical Image Analysis, vol.5 ,pp.143–156, 2001.

[59] R. P. Woods, S. R. Cherry, and J. C. Mazziotta, "Rapid automated algorithm for alignment and reslicing PET images", Journal Computer Assisted Tomography, vol.16, pp.620–633. 1992.

[60] R. P. Woods, S. T. Grafton, C. J. Holmes, S. R. Cherry, and J. C. Mazziotta, "Automated image registration, I: General methods and intrasubject, intramodality validation", Journal Computer Assisted Tomography vol. 22, pp.141–154. 1998.

[61] R. P. Woods, J. C. Mazziotta, and S. R. Cherry, "MRI-PET registration with automated algorithm", Journal Computer Assisted Tomography, vol. 17:4 pp.536–546. 1993.

[62] M. Jenkinson, S. Smith, "A global optimisation method for robust affine registration of brain images", Medical Image Analysis vol. 5, pp.143–156, 2001.

[63] J. Mark and S. Smith, "Optimisation in Robust Linear Registration of Brain Images" FMRIB Technical Report TR00MJ2.

[64] M. M. Sung, H. J. Kim, E. K Kim, J. Y. Kwak, J. K. Yoo, and H. S. Yoo, "Clinical Evaluation of JPEG2000 Compression for Digital Mammography", IEEE Transaction on Nuclear Science, vol. 49, no. 3, June 2002.

[65] J. P. W. Pluim, J. B. A. Maintz and M. A. Viergever, "Mutual information based registration of medical images: a survey", vol. 22, no. 8, August 2003.

[66] C. E. Shannon, "A mathematical theory of communication," Bell System Technical. Journal, vol. 27, pp. 379–423/623–656, 1948.

[67] H. Abdi, L. J. Williams, “Tukey's Honestly Significant Difference (HSD) Test”, Encyclopedia of Research Design, 2010.

[68] D. L. Hill, C. Studholme, D. J. Hawkes, “Voxel similarity measures for automated image registration”, Visualization in Biomedical Computing Richard A. Robb; Ed, Proc. SPIE vol. 2359, pp. 205-216, 1994.

[69] D. L. G. Hill, D. J. Hawkes, N. A. Harrison and C. F. Ruff, “A strategy for automated multimodality image registration incorporating anatomical knowledge and imager characteristics”, Information Processing in Medical Imaging, vol. 687, pp.182-196, 1993.

[70] M. Unser, A. Aldroubi, and M. Eden, “Polynomial spline signal approximations: Filter design and asymptotic equivalence with Shannon’s sampling theorem,” IEEE Transactions on Information Theory, vol. 38, pp. 95–103, 1992.

[71] M. Unser, A. Aldroubi, and M. Eden, “B-spline signal processing: Part I—Theory,” IEEE Transactions on Signal Processing, vol. 41, no. 2, pp. 821–833, 1993.

[72] M. Unser, A. Aldroubi, and M. Eden, “B-spline signal processing: Part II—Efficient design and applications,” IEEE Transactions on Signal Processing, vol. 41, no. 2, pp. 834–848, 1993.

[73] M. Unser, A. Aldroubi, and M. Eden, “Fast B-splines transforms for continuous image representation and interpolation,” IEEE Transactions on Pattern Analysis Machine Intelligence, vol. 13, pp. 277–285, 1991.

[74] A. Amanatiadis and I. Andreadis, “A survey on evaluation methods for image interpolation”, Measurement Science and Technology, vol 20, pp. 104015, 2009.

[75] M. Holden, D. L. G. Hill, E. R. E. Denton, J. M. Jarosz, T. C. S. Cox, T. Rohlfing, J. Goodey, and D. J. Hawkes, “Voxel Similarity Measures for 3-D Serial MR Brain Image Registration”, IEEE Transactions on Medical Imaging, vol. 19, no. 2, February 2000.

[76] N. H. Kashou, “A Novel Method for Increasing Resolution based on Original Information in MR Datasets”, unpublished.

[77] O. D. Evans and Y. Kim, “Efficient implementation of image warping on a multimedia processor,” Real-Time Imaging Journal, vol. 4, pp. 417–428, 1998.

[78] J. Ashburner, K. F. W. Penny, Human Brain Function, 2nd edition, Chapter 2, pp 3.

[79] J. L. Ostuni, A. K. S. Santha, V. S. Mattay, D. R. Weinberger, R. L. Levin, J. A Frank, "Analysis of interpolation effects in the reslicing of functional MR images" Journal of Computer Assisted Tomography, vol. 21, pp.803-810, 1997.

[80] HW. Venema , SS . Phoa , PG. Mirck , FJ. Hulsmans, CB. Majoie, B Jr. Verbeeten "Petrosal Bone: Coronal Reconstructions from Axial Spiral CT Data Obtained with 0.5-mm Collimation Can Replace Direct Coronal Sequential CT Scans", Radiology, vol 213, pp. 375-382. November 1999.

[81] J. V. Hajnal, N. Saeed, E. J. Soar, A. Oatridge, I. R. Young, G. M. Bydder, "A registration and interpolation procedure for subvoxel matching of serially acquired MR images" Journal Computer Assisted Tomography, vol.19, pp.289-296, 1995.

[82] L.G. Brown, "A Survey of Image Registration Techniques, ACM Computing Surveys", vol.24, pp.325–376, December 1992.

[83] J. B. A. Maintz and M. A.. Viergever, "A Survey of Medical Image Registration", Medical Image Analysis, vol.2, pp.1–36. 1998.

[84] C. R. Maurer and J. M. Fitzpatrick, "A Review of Medical Image Registration, chapter in Interactive Image-Guided Neurosurgery", American Association of Neurological Surgeons, Park Ridge, IL, 1993.

[85] F. Maes, "Segmentation and registration of multimodal medical images: from theory, implementation and validation to a useful to tool in clinical practice", PhD thesis, Catholic University of Leuven, Belgium, 1998.